

**This item is the archived peer-reviewed author-version of:**

Carbon bed post-plasma to enhance the CO<sub>2</sub> conversion and remove O<sub>2</sub> from the product stream

**Reference:**

Girard-Sahun Fanny, Biondo Omar, Trenchev Georgi, van Rooij Gerard, Bogaerts Annemie.- Carbon bed post-plasma to enhance the CO<sub>2</sub> conversion and remove O<sub>2</sub> from the product stream  
Chemical engineering journal - ISSN 1873-3212 - 442(2022), 136268  
Full text (Publisher's DOI): <https://doi.org/10.1016/J.CEJ.2022.136268>  
To cite this reference: <https://hdl.handle.net/10067/1882860151162165141>

# Carbon bed post-plasma to enhance the CO<sub>2</sub> conversion and remove O<sub>2</sub> from the product stream

*Fanny Girard-Sahun<sup>1,\*</sup>, Omar Biondo<sup>1,2,\*</sup>, Georgi Trenchev<sup>1</sup>, Gerard van Rooij<sup>2,3</sup> and Annemie Bogaerts<sup>1</sup>*

<sup>1</sup>Research Group PLASMANT, Department of Chemistry, University of Antwerp, Universiteitsplein 1, Wilrijk B-2610, Belgium

<sup>2</sup>DIFFER, 5612AJ Eindhoven, The Netherlands

<sup>3</sup>Faculty of Science and Engineering, Maastricht University, 6229 GS Maastricht, The Netherlands

\*Shared first author

Corresponding authors:

Dr Fanny Girard-Sahun, email: [fanny.girard-sahun@uantwerpen.be](mailto:fanny.girard-sahun@uantwerpen.be)

M. Sc Omar Biondo, email: [omar.biondo@uantwerpen.be](mailto:omar.biondo@uantwerpen.be)

Prof. Annemie Bogaerts, email: [annemie.bogaerts@uantwerpen.be](mailto:annemie.bogaerts@uantwerpen.be)

## Abstract

CO<sub>2</sub> conversion by plasma technology is gaining increasing interest. We present a carbon (charcoal) bed placed after a Gliding Arc Plasmatron (GAP) reactor, to enhance the CO<sub>2</sub> conversion, promote O/O<sub>2</sub> removal and increase the CO fraction in the exhaust mixture. By means of an innovative (silo) system, the carbon is constantly supplied, to avoid carbon depletion upon reaction with O/O<sub>2</sub>. Using this carbon bed, the CO<sub>2</sub> conversion is enhanced by almost a factor of two (from 7.6 to 12.6 %), while the CO concentration even increases by a factor of three (from 7.2 to 21.9 %), and O<sub>2</sub> is completely removed from the exhaust mixture. Moreover, the energy efficiency of the conversion process drastically increases from 27.9 to 45.4 %, and the energy cost significantly drops from 41.9 to 25.4 kJ.L<sup>-1</sup>. We also present the temperature as a function of distance from the reactor outlet, as well as the CO<sub>2</sub>, CO and O<sub>2</sub> concentrations and the temperature in the carbon bed as a function of time, which is important for understanding the underlying mechanisms. Indeed, these time-resolved measurements reveal that the initial enhancements in CO<sub>2</sub> conversion and in CO concentration are not maintained in our current setup. Therefore, we present a model to study the gasification of carbon with different feed gases (i.e., O<sub>2</sub>, CO and CO<sub>2</sub> separately), from which we can conclude that the oxygen coverage at the surface plays a key role in determining the product composition and the rate of carbon consumption.

Indeed, our model insights indicate that the drop in CO<sub>2</sub> conversion and in CO concentration after a few minutes is attributed to deactivation of the carbon bed, due to rapid formation of oxygen complexes at the surface.

## Keywords

CO<sub>2</sub> conversion / gliding arc plasma / carbon bed / oxygen removal / gas separation / CO enrichment

## Nomenclature

### Latin letters

A	cross-sectional area (cm <sup>2</sup> )
a	stoichiometric coefficient
B	active site density (mol.m <sup>-2</sup> )
b	fitting parameter
C <sub>surf</sub>	active site density (cm <sup>-3</sup> )
C(s)	active carbon site
C(s)-O	oxygen atom chemisorbed at an active carbon site
EC	energy cost (kJ.L <sup>-1</sup> )
h	Planck constant (J.s)
ΔH <sup>o</sup> <sub>R</sub>	standard reaction enthalpy (kJ.mol <sup>-1</sup> )
k	reaction rate coefficient
k <sub>B</sub>	Boltzmann constant (J.K <sup>-1</sup> )
m	mass of one molecule (kg)
N <sub>A</sub>	Avogadro number (mol <sup>-1</sup> )
n	number density
P	power (kW)
P	pressure (Pa)
Q <sub>in</sub>	input flow rate (mol.min <sup>-1</sup> )
Q <sub>out</sub>	output flow rate (mol.min <sup>-1</sup> )
R	ideal gas constant (L.atm.K <sup>-1</sup> .mol <sup>-1</sup> )
R	reaction rate
SEI	specific energy input (kJ.mol <sup>-1</sup> )
T	temperature (K)
Td	Townsend; 1 Td = 10 <sup>21</sup> V.m <sup>-2</sup>
V <sub>m</sub>	molar volume at atmospheric pressure and room temperature (L.mol <sup>-1</sup> )
V	volume (cm <sup>3</sup> )
X	conversion (%)
x	position in the simulated reactor

### Greek letters

$\pi$	pi number
$\Pi$	product

### *Abbreviations*

APS	Advanced Plasma Solutions
BET	Brunauer-Emmett-Teller
CAPEX	Capital expenditure
CCS	CO <sub>2</sub> capture and storage
CCU	CO <sub>2</sub> capture and utilization
DBD	dielectric barrier discharge
DFT	density functional theory
eV	electronvolt
GAP	gliding arc plasmatron
GC	gas chromatography
MW	microwave
NDIR	non-dispersive infrared spectroscopy
OGSH	offshore geological storage of hydrogen
OPEX	operating expenses
RBR	reverse Boudouard reaction
RGA	residual gas analysis
SEM	scanning electron microscopy
TCD	thermal conductivity detector
TGA	thermogravimetric analysis
TGA-MS	thermogravimetric analysis coupled with mass spectrometry
TSA	total surface area
0D	zero-dimensional

### *Superscripts*

L	left-hand side
R	right-hand side

### *Subscripts*

bed	carbon bed
corr	corrected for the gas expansion
0	Initial
j	reaction j
in	Input
l	reactants of reaction j
out	Output
s	Species
surf	Surface

## **1. Introduction**

Due to the high CO<sub>2</sub> levels in the atmosphere (more than 410 ppm [1]), we need to find urgent solutions for reducing CO<sub>2</sub> emissions in our fight against global warming. Since 2015, with the Paris agreement, there have been multiple efforts towards the implementation of low-carbon energy production, in order to pursue the net-zero target, in at least 20 countries in the world. A net-zero emissions energy system does not add any CO<sub>2</sub> to the atmosphere [2]. There are different ways of approaching the issue of reducing CO<sub>2</sub> emissions. For instance, H<sub>2</sub> has the highest possible energy density and its use features CO<sub>2</sub>-free emissions. However, hydrogen-based energy production is limited by the storage capacity of the available facilities, due to the very low volumetric density of hydrogen. Such a drawback can be overcome with the development of the offshore geological storage of hydrogen (OGSH) in sub-sea reservoirs [3]. Alternatively, CO<sub>2</sub> can be either captured and stored (known as CCS) or captured and utilized into valuable chemicals, useful for a wide range of industrial applications. This approach, known as “CCU - CO<sub>2</sub> Capture and Utilization” is very promising, as CO<sub>2</sub> becomes then a renewable resource of energy for various applications. Especially, CO<sub>2</sub> utilization as feedstock for fuels represents a major route for decarbonization [1].

Direct CO<sub>2</sub> splitting (equation (1)) is highly endothermic and requires a lot of energy in thermo-catalytic processes, i.e. temperatures of at least 2000 K at atmospheric pressure [4]. In this context, plasma technology is a very promising candidate to face this challenge [4]. Due to its unique and highly-reactive composition (high-energy free electrons, excited molecules/atoms, radicals and ions, as well as photons), plasma offers a route to convert CO<sub>2</sub> with high energy efficiency and operation flexibility, and at mild conditions (ambient pressure and temperature), as demonstrated in numerous studies [5]. For instance, pure CO<sub>2</sub> dissociation was investigated with dielectric barrier discharges (DBD), which are one of most common types of non-thermal plasmas for CO<sub>2</sub> conversion [4,6,7]. Notwithstanding this, DBDs provide low energy efficiency (around 10%) [4]. Under typical conditions for DBDs, i.e. reduced electric field of 200 Td (Townsend; 1 Td = 10<sup>-21</sup> V m<sup>2</sup>) [4] and electron temperature higher than 5 eV [8], only ca. 10% of the electron energy is deposited into the CO<sub>2</sub> vibrational degrees of freedom, which are known to promote dissociation through the most efficient pathway [4]. Therefore, intensive research has been conducted on the applicability of so-called “warm” plasmas, which are plasmas with a high degree of equilibrium between vibrational and translational degrees of freedom. The particular conditions of operation of these plasmas allow combining advantages of both thermal (high gas temperature) and non-thermal (vibrational excitation) systems [4,9]. With this aim, “warm” plasmas such as microwave (MW) plasmas [10–12], (2D) gliding arc plasma [13,14] or (3D) gliding arc plasmatron at atmospheric pressure [14-16], were investigated for more efficient CO<sub>2</sub> conversion, providing promising results. Recently, an atmospheric pressure glow discharge [15] was also proposed as an interesting technology for CO<sub>2</sub> dissociation, offering a conversion degree of up to 12% and energy efficiencies reaching 30%. Additionally, the conversion of CO<sub>2</sub> mixed with N<sub>2</sub>, which is a typical impurity of waste streams and which can promote CO<sub>2</sub> vibrational excitation through efficient vibrational exchanges [16,17], was also studied in gliding arc reactors [18,19] and in a DBD reactor [20].

The dissociation of CO<sub>2</sub> leads to the formation of CO and an oxygen atom, and is a highly endothermic reaction, requiring a considerable amount of energy.

, With (1)

The CO produced can be used in e.g., the Fischer-Tropsch process to produce liquid hydrocarbons. Currently, plasma technology for CO<sub>2</sub> conversion is still at low technological readiness level (TRL 3-4; lab scale). However, plasma is a well-established technology for lighting, surface cleaning, etching, film deposition and polymerization at industrial level [21,22]. Moreover, non-thermal plasma stands out as a promising alternative to the widely used oxidation processes for water and flue gas treatment [23] and can be a suitable tool for nanomaterial processing, analytical chemistry, sterilization, disinfection, medicine and food safety [24].

More recently, another possible route for CO<sub>2</sub> conversion using biochar as a solid reactant is being investigated, also called CO<sub>2</sub> gasification of biochar [25]. Biochar is obtained from pyrolysis of biomass and it is a quite cheap renewable energy source [26]. With this in mind, and provided that the system is powered by electricity coming from renewable sources, we consider CO<sub>2</sub> gasification of biochars a promising candidate to bolster the efforts towards a net-zero energy system. Furthermore, gasification of coal is a well-known process for the production of CO and syngas. We believe that the combination of these technologies can bring a novel, highly efficient solution to the market. The reaction of CO<sub>2</sub> with carbon is known as the Reverse Boudouard Reaction (RBR) (equation (2)) [27]:

, With (2)

At atmospheric pressure, the RBR also requires high temperatures (> 700°C) [27]. Several gasification heat sources to favour the RBR rate have been studied, e.g. conventional convective heating [27], solar-driven gasification [27] and microwave-driven CO<sub>2</sub> gasification [28–30]. Especially MW heating [28–30] allowed to decrease the activation energy for CO<sub>2</sub> gasification by 60-70% and to reach energy efficiencies of 45% at laboratory scale [31]. Recently, a few groups investigated the RBR with solid carbon driven by different kinds of plasmas and showed very interesting results [32–34].

Overall, one should consider that O<sub>2</sub>-free exhaust gas is needed from CO<sub>2</sub> splitting (i.e., ideally pure CO) to be directly used in industrial applications, like the Fischer-Tropsch process as mentioned above. Indeed, CO<sub>2</sub> splitting results in CO and O, and the latter will (1) recombine to form O<sub>2</sub>, but also (2) be responsible for unwanted back-reactions (CO + O) to produce again CO<sub>2</sub> [35], lowering the net CO<sub>2</sub> conversion and energy efficiency. In addition, also O<sub>2</sub> can give rise to back-reactions with CO into CO<sub>2</sub>. Therefore, both O and O<sub>2</sub> are undesirable species that need to be either physically or chemically quenched to avoid reverse reactions, reduce separation costs downstream and increase the energy efficiency [6,36,37]. Only a few methods are described in literature, such as the use of hollow fiber membranes

permeable to  $O/O_2$ , which is then removed using a sweep gas [38]. A promising route, also mentioned above, is to use solid carbon after the plasma reactor, which can be oxidized by  $O$  and/or  $O_2$  to produce  $CO$ , allowing (i) to consume the undesirable  $O/O_2$  and (ii) to enrich the exhaust in  $CO$ , beneficial for the applications.

In this work, we investigate the conversion of  $CO_2$  by a Gliding Arc Plasmatron (GAP) in combination with a carbon bed after the plasma reactor, to promote  $O/O_2$  removal and increase the  $CO$  fraction in the exhaust mixture. Although the plasma method requires quite some energy, it uses electricity, and is quickly switched on/off, so it is very suitable for combination with renewable electricity. Moreover, we demonstrated already high energy efficiency for plasma-based  $CO_2$  conversion in this GAP [39]. The combination with carbon bed will further improve the performance. We present an innovative design, in which the carbon is constantly supplied over time by a silo system, to avoid carbon depletion upon reaction with  $O/O_2$ . The carbon bed is put in direct contact with the afterglow of the gliding arc plasma produced in pure  $CO_2$  at atmospheric pressure, for maximum effect. During the process, the temperature is recorded as a function of time directly in the carbon bed, providing useful information for a better understanding of the underlying mechanisms. Furthermore, the exhaust gas composition is analysed by a combination of gas chromatography and optical sensors. The performance of the GAP with carbon bed is determined and compared with the benchmark (i.e. without carbon bed).

Although it has been experimentally proven that carbonaceous materials are effective options to increase the selectivity towards  $CO$  in the  $CO_2$  splitting process, more insight is needed to demonstrate its full potential and identify the relevant underlying mechanisms. In this respect, modelling is a very useful tool to unravel chemical pathways especially when these are inaccessible experimentally. Zero-dimensional (0D) chemical kinetic models, also referred to as global models, are the method of choice to study the contributions of different chemical reactions occurring in plasma ignited in complex gas mixtures [40]. Therefore, in addition to our experimental work, we examine here the gasification process occurring when a reactive gas mixture produced by a plasma comes in contact with a carbon bed. This analysis involves the construction and the validation of a 0D chemical kinetics model against experiments. The validation of a model is a crucial aspect and requires particular experimental conditions, in order to minimize the number of assumptions under which the predictions are valid. With this in mind, we have chosen to validate our model with the gasification experiments presented by Panerai *et al.* [41], under pure  $O_2$  and  $CO_2$  atmospheres, respectively, in order to get insights into the reaction pathways for carbon oxidation in the presence of  $O_2$ ,  $CO_2$  and  $CO$  and the deactivation of the carbon bed, with consequent decrease in selectivity towards the latter. This model greatly helps us to explain our experimental results, as will be described in detail in this paper. To resume, the innovations of this work, compared to [32–34], are: i) the use of a silo system, to avoid carbon depletion due to gasification; ii) time-resolved temperature measurements in the carbon bed; iii) a combination of gas chromatography and optical sensors to

determine the exhaust composition as a function of time; iv) and especially coupling our experiments with detailed kinetic modelling, to provide detailed insights into the underlying chemistry and the deactivation of the carbon bed.

## 2. Experimental section

### 2.1. Experimental setup

We performed our experiments in a gliding arc plasmatron (GAP) originally developed by Nunnally *et al.* [42] and previously described by our group [39]. We used pure CO<sub>2</sub> as reactant gas in the plasma reactor (Air Liquide, purity 99.995%; flow rate kept constant at 10 ). The flow rate was adjusted with a Bronkhorst mass flow controller. The cathode and anode (stainless steel) were connected to an AC current source-type power supply (AFS) and to the ground, respectively. Electrode degradation (e.g., due to ablation) was very limited at the conditions under study. Indeed, this AC power supply reduces the thermal stress on the developing cathode spots. Furthermore, we utilize a strongly turbulent internal gas flow, which efficiently cools down the electrodes. Voltage and current were measured by using a high-voltage probe (Cal Test Electronics CT4028) and a current sense resistor (2 Ω) connected to a two-channel digital oscilloscope (Keysight DSOX1102G). Based on the product of measured voltage and current, we calculated the power injected in the plasma. The plasma arc was formed between both electrodes, as previously described [39], and can also partly leave the reactor through the anode (reactor outlet) [43], forming an afterglow in contact with the carbon bed, placed at the anode exhaust.

The general scheme, including the GAP plasma reactor, the carbon bed and the silo, is illustrated in Figure 1A, and a picture is given in Figure 1B.

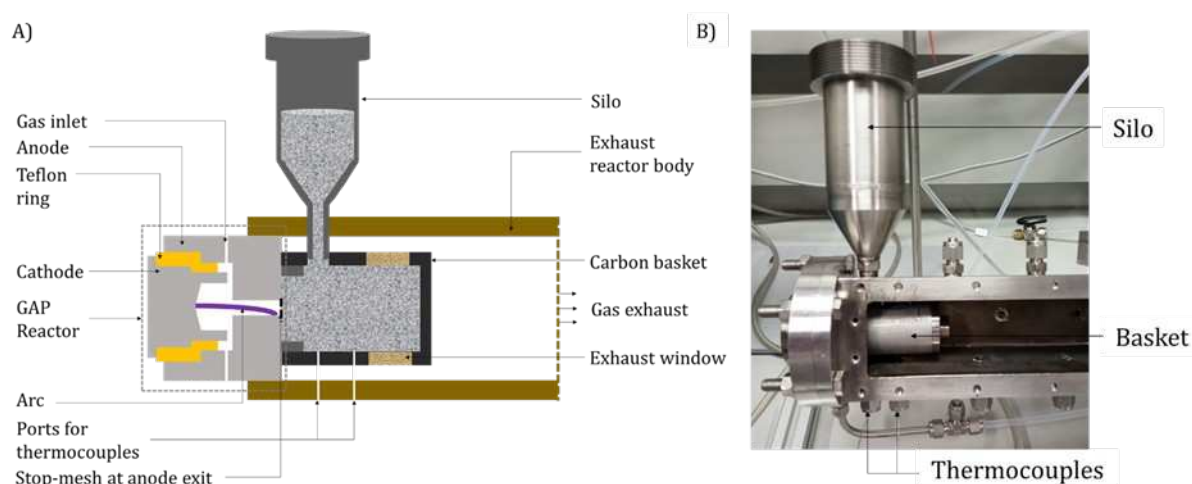


Figure 1. Scheme (A) and picture (B) of the GAP plasma reactor setup, including the carbon basket and silo. Note: The scheme is not at scale.



The carbon basket is directly attached to the anode. The silo containing spare carbon is attached to the basket through the exhaust reactor body. A metallic mesh is used at the anode exit to keep the carbon pellets out of the plasma reactor. Two dedicated ports allow to measure the temperature inside the carbon bed, at 15 and 35 mm from the anode exit; see Figure 2 below.

The reactor outlet (length 26 mm and inner diameter 7.07 mm, see pictures in Supporting Information (SI): Figure S1) was designed so that the contact of the plasma afterglow and the carbon bed is maximized: the aperture on the basket side is wider (see Figure S1(C) in SI), so that the carbon can get closer to the arc, which improves the contact between active plasma species and the carbon, and also takes benefit of the high temperature of the arc (3000 K according to computer simulations) [44].

The basket was filled with ca. 5 g of carbon pellets for each plasma run. We used two different types of commercial carbon materials of different quality and particle size: activated charcoal Norit PK 1-3 (Sigma Aldrich, 1-3 mm typical pellet size, from peat, steam activated; named “charcoal 1” in the figures below) and untreated activated charcoal C3014 (Sigma Aldrich, typical pellet size of 250-850  $\mu\text{m}$ ; named “charcoal 2”). Note that there is a very wide variety of commercial carbon samples available in the market. The particle size is usually the main (even sometimes the only one) parameter given by carbon suppliers. Therefore, it is the easiest way to investigate differences among the wide range of carbon samples available. In future work, we plan to also compare carbon samples with the same particle size but different specific surface area and morphology, if available. The surface area of charcoal 1 and charcoal 2, as received, was estimated by  $\text{N}_2$ -Brunauer-Emmett-Teller (BET) measurements to be  $705 \pm 71$  and  $703 \pm 70 \text{ m}^2 \text{ g}^{-1}$ , respectively (see section 2.2. for details on the technique). The surface area of charcoal 1 was also measured after 7 minutes of treatment, in order to estimate the surface variation resulting from gasification reactions. The morphology of the charcoals as received, as well as after the gasification reactions, was investigated by Scanning Electron Microscopy (SEM-see section 2.2.). The collected images are reported in the Supporting Information (SI), in Figure S2.

A silo (stainless steel) containing fresh carbon was inserted inside the basket through the post-plasma reactor tube, to provide a continuous source of carbon during the reaction and avoid carbon depletion upon reaction with  $\text{O}/\text{O}_2$  (within the limits of the carbon volume contained in the silo, i.e., approx.  $200 \text{ cm}^3$ , see Figure 1A). It can be refilled with carbon through an opening on its top (Figure 1B). A mesh (stainless steel) was added at the anode exit to hold the carbon pellets inside the basket and avoid disturbing the arc inside the plasma reactor by creating a short circuit. In

addition, the temperature in the carbon bed during operation was measured by means of two thermocouple ports along the basket (see Figure 1A-B).

Filters were placed on the exhaust line to make sure that the charcoal/ash particles did not enter the gas analytic equipment. The exhaust gas composition ( $\text{CO}_2$ ,  $\text{CO}$  and  $\text{O}_2$ ) was analysed online by NDIR (Non-Dispersive Infrared Spectroscopy, for  $\text{CO}_2$  and  $\text{CO}$ ) and by an optical oxygen sensor (for  $\text{O}_2$ ). Besides, the exhaust gas mixture was also analysed by gas chromatography (GC); see next section.

The post-plasma reactor tube was designed specifically for the purpose of these experiments, i.e., (1) to accommodate the carbon basket combined with the silo, and (2) to measure the temperature in the post-plasma region as a function of distance from the reactor outlet, thanks to several ports for thermocouples. Indeed, to determine the best position of the carbon bed after the plasma at our operating conditions, we first measured the temperature profile in the post-plasma reactor tube with K-type thermocouples with four-channels type data loggers (Thermosense) in a free-reactor (i.e., without carbon bed; see Figure 2).

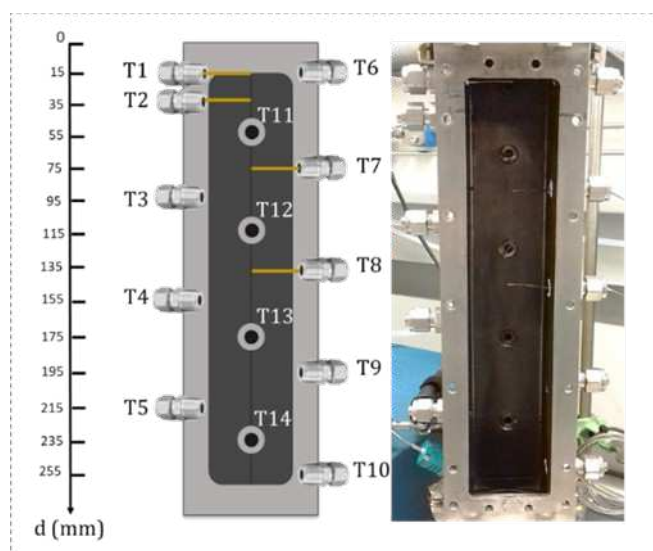


Figure 2. Scheme (left) and picture (right) of the post-plasma reactor tube with several ports for the K-type thermocouples (named  $T_x$ , with  $x = 1$  to 14). The “zero” position corresponds to the reactor outlet (anode exit position). T1 and T2 (at 15 and 35 mm) measure the temperature inside the carbon bed; cf. Figure 1)

## 2.2. Carbon materials characterization techniques

The carbon materials (namely charcoal 1 and 2) used in this study were characterized by Brunauer-Emmett-Teller (BET) analysis, Scanning Electron Microscopy (SEM) and Thermogravimetric Analysis coupled with Mass Spectrometry (TGA-MS).

The specific surface area of charcoal 1 and 2 was calculated by the BET method. Prior to the measurements, the samples were degassed for 16 hours under vacuum at 200 °C. The sorption was then performed under N<sub>2</sub> atmosphere using a Quantachrome Quadrasorb SI.

For SEM analysis, an FEI Quanta 250 FEG scanning electron microscope was used. It was operated at 20 kV and the secondary electron detector was used to generate the images. The working distance (distance between the sample and the polepiece, i.e. the last lens of the imaging system; "WD") is given in the bar below every image and was always between 8 and 10 mm. To prepare the sample, a chunk of the charcoal was attached to the aluminium SEM stub using double sided carbon tape. No further treatment of the sample was needed (like coating or crushing).

Thermogravimetric analysis (TGA) was used for studying the thermal properties of the activated charcoal, using a Mettler Toledo TGA-DSC 3+. The measurement was performed under a continuous flow of argon or oxygen i.e. 100 mL/min (80 mL/min protective gas to protect the balance + 20 mL/min purge gas). The sample was first flushed 45 min at 30 °C to remove all the air from the oven, and then heated up from 30 to 1000 °C with a heating rate of 10 °C/min. An alumina crucible of 150 µL was used. TGA was associated with a mass spectrometer to analyse the products from charcoal pyrolysis. The detection of the gaseous products was performed with a HPR-20 R&D (Hiden) mass spectrometer, controlled by EGAsoft software. The following settings were used: an electron voltage of 70 eV and an emission current of 400 mA. An electron multiplier (SEM) detector was used to scan m/z from 1 to 19, from 21 to 39 and from 42 to 120.

### **2.3. Gas analysis techniques**

The exhaust gas mixture was analysed via various analytical techniques, to ensure the accuracy of the measurements. Non-dispersive Infrared Spectroscopy (NDIR) (X-STREAM Enhanced General Purpose Process Gas Analyzer (XEGP) from Emerson) was used to analyse in real time the CO<sub>2</sub> and CO concentration profiles. Furthermore, we used a specific optical oxygen gas sensor (FDO<sub>2</sub>, Pyroscience science technology) to measure the O<sub>2</sub> concentration continuously over time. We always started the measurements before plasma ignition, to first measure the blank composition, needed for the conversion calculation (i.e., 100 % CO<sub>2</sub>). All measurements were performed in triplicate.

In addition, we also analysed the exhaust gas with a three-channels compact gas chromatograph from Interscience. Each channel leads to a different column and detector. Two channels were used for this study: (1) carboxen and molsieve columns (1010 PLOT and 5A, respectively) were used to separate the permanent gases, such as O<sub>2</sub>, N<sub>2</sub> and CO, further detected with a Thermal Conductivity Detector (TCD); and (2) two RT Q-bond columns (3 m and 10 m length, respectively) were used for the pre-separation and separation of CO<sub>2</sub> from the permanent gases, leading to a

second TCD. The concentrations of the different products were calculated based on prior calibration of the GC in the concentration ranges of interest. As the GC analyses a sample immediately after sampling, a waiting time of about 6 minutes (time to get the chromatogram) was needed between one measurement and another. Moreover, this technique does not allow on-time measurements. Therefore, we compared the optical measurements (NDIR and optical O<sub>2</sub> sensor) with the GC measurements, to ensure their accuracy and to eventually use them for calculating the performance of the GAP with carbon bed in terms of CO<sub>2</sub> conversion and CO and O<sub>2</sub> concentrations.

#### 2.4. Performance calculations

The conversion of CO<sub>2</sub> is usually defined as:

$$(3)$$

With  $C_{CO_2, blank}$  and  $C_{CO_2, plasma}$  the CO<sub>2</sub> concentrations in the blank (without plasma) and during plasma, respectively (in %).

However, pure CO<sub>2</sub> splitting results in the expansion of the gas ( $V_{exp}$ ) i.e., 1 molecule of CO<sub>2</sub> produces 1.5 molecules after (complete) reaction. In presence of a carbon bed, possible heterogeneous reactions between CO<sub>2</sub>/O<sub>2</sub>/O/CO and solid carbon might also occur, contributing even more to the gas expansion effect [34]. As a consequence, the exhaust gas flow rate is higher than the initial flow rate and all species are diluted in a higher volume than the initial one, i.e., the CO<sub>2</sub> concentration in the final volume appears lower than it would be in the initial volume without expansion, resulting in an apparent higher conversion. Therefore, we need to know the exhaust flow rate, to correct the conversion from gas expansion. For this purpose, we used the method by Huang et al., [34]:

$$(4)$$

With  $F_{CO_2, inlet}$  and  $F_{CO_2, outlet}$  the CO<sub>2</sub> flow rates at the inlet and outlet, respectively .

$F_{O_2, outlet}$  is determined based on the oxygen balance of the gas mixtures in the inlet and outlet [34]:

$$(5)$$

Besides the CO<sub>2</sub> conversion and the CO and O<sub>2</sub> concentrations in the exhaust mixture, we also calculated the energy efficiency and energy cost for our experiments. For this purpose, we need to know the specific energy input (SEI). The latter is the ratio of power over flow rate, and is defined as:

$$(6)$$

With the power delivered into the plasma (kW), the inlet CO<sub>2</sub> flow rate ( $\dot{V}$ , 60 is the number of seconds per minute) and the molar volume at atmospheric pressure and room temperature (24.5 l/mol).

The energy efficiency is defined as:

$$(7)$$

Based on our modelling insights, we expect the reverse Boudouard reaction to play only a minor role in the chemistry at the conditions under study. Therefore, the  $\dot{V}$  used in the calculation refers to pure CO<sub>2</sub> splitting, i.e.,  $\dot{V} = 283$  l/min (cf. Equation (1)). See sections 4.1, 4.5 and 4.6 for further discussion.

Finally, the energy cost of the CO<sub>2</sub> conversion process is defined as:

$$(8)$$

### 3. Model description

We applied a zero-dimensional (0D) chemical kinetics model, using ZDPlasKin [45]. This model solves the continuity equations for the different plasma species

$$(9)$$

in which  $n_s$  refers to the density of the species  $s$ ,  $x$  is the position in the simulated reactor, index  $j$  refers to reaction  $j$  and index  $l$  refers to the different reactants of reaction  $j$ .  $\nu_{s,j}$  and  $\nu_{s,l}$  are the right- and left-hand side stoichiometric coefficients of species  $s$ , respectively, taking part in reaction  $j$ ,  $k_j$  is the reaction rate coefficient, and  $R_j = k_j \prod n_l^{\nu_{s,l}}$  is the reaction rate, with  $\prod$  being the product of densities  $n_l$  of species present on the left side of reaction  $j$ .

#### 3.1. Chemistry set

The species in our model are listed in Table 1.

Table 1. Species described in the model.

Gas-phase ground state species
CO <sub>2</sub> , CO, O <sub>2</sub> , O, C
Surface species
C(s), C(s)-O

<sup>a</sup> C(s) and C(s)-O represent an active carbon site and an oxygen atom chemisorbed at an active carbon site, respectively.

The concept of active surface site entails that heterogeneous reactions occur only at specific sites on which oxygen is adsorbed and forms complexes, which may ultimately lead to desorption of products, such as CO or CO<sub>2</sub>. For carbonaceous materials, the active surface sites can be identified as structural features, such as defects in carbon layer planes and edge carbon atoms, disordered carbon atoms, heteroatoms (O,S,N) and mineral matter [46].

Prata *et al.* [47] applied the concept of active surface site to the modeling of the gas-surface reactions relevant for the ablative heat shield occurring during spacecraft atmospheric re-entry. We have chosen the chemical reaction set proposed by Prata amongst the other available sets [48–50], since it provides the most complete description for carbon oxidation reactions, along with a better agreement with experimental trends. The reaction set for the carbon oxidation is detailed in Table 2.

Table 2. Heterogeneous reactions and their rate coefficients taken from Prata *et al.* [47] for solid carbon oxidation.

Reaction	Rate constant	Units
O(g) + C(s) ⇌ C(s)-O (O chemisorption)		[cm <sup>3</sup> s <sup>-1</sup> ]
C(s)-O ⇌ O(g) + C(s) (O desorption from mobile sites)		[s <sup>-1</sup> ]
C(s)-O ⇌ O(g) + C(s) (O desorption from immobile sites)		[s <sup>-1</sup> ]
C(s)-O + M ⇌ CO(g) + M M = O, O <sub>2</sub> , CO, CO <sub>2</sub> (Collision-induced CO desorption)		[cm <sup>3</sup> s <sup>-1</sup> ] <sup>a,b</sup>
O <sub>2</sub> (g) + C(s) ⇌ O(g) + C(s)-O (O <sub>2</sub> partial chemisorption)		[cm <sup>3</sup> s <sup>-1</sup> ] <sup>c</sup>
O <sub>2</sub> (g) + 2 C(s) ⇌ 2 C(s)-O (O <sub>2</sub> chemisorption)		[cm <sup>6</sup> s <sup>-1</sup> ]
2 C(s)-O ⇌ O <sub>2</sub> (g) + 2 C(s) (O <sub>2</sub> desorption from mobile sites)		[cm <sup>3</sup> s <sup>-1</sup> ]
2 C(s)-O ⇌ O <sub>2</sub> (g) + 2 C(s) (O <sub>2</sub> desorption from immobile sites)		[cm <sup>3</sup> s <sup>-1</sup> ]
O(g) + C(s)-O ⇌ CO <sub>2</sub> (g) (C(s)-O oxidation – only from mobile sites)		[cm <sup>3</sup> s <sup>-1</sup> ] <sup>d</sup>
O <sub>2</sub> (g) + C(s)-O ⇌ CO <sub>2</sub> (g) + O(g) (CO <sub>2</sub> desorption – only from mobile sites)		[cm <sup>3</sup> s <sup>-1</sup> ] <sup>d</sup>

<sup>a</sup>activation energy increased from 4000 K [47] to 6000 K, pre-exponential factor lowered from 100 [47] to 1 for the mobile sites and from 1000 to 1 for the immobile sites (see motivations in text).

<sup>b</sup>added also CO and CO<sub>2</sub> as collision partners, according to the Eley-Rideal model described in Prata [47].

<sup>c</sup>added to the reaction set from the model by Zhluktov and Abe [49] (see text), not included in Prata [47], for studying its effects in the model predictions.

<sup>d</sup>activation energy increased from 500 K (Prata) to 2000 K, as suggested by Zhluktov and Abe [49] (see text).

In this table,  $B$  is the active site density (in mole per square meter),  $k_B$  is the Boltzmann constant [J / K],  $h$  is the Planck constant [J · s],  $m_O$ ,  $m_{O_2}$ ,  $m_{CO}$  and  $m_{CO_2}$  are the O, O<sub>2</sub>, CO and CO<sub>2</sub> mass in kg, respectively. Note that  $V/A$  is the ratio between the carbon bed volume and the carbon surface area and it is calculated according to the experimental conditions (hence: in our model here adopted from the data of Prata [47]).

In our study we keep the assumption of two different types of oxygen chemisorption, namely mobile for weakly bonded oxygen (single-bond character C-O) and immobile for strongly bonded oxygen (double-bond character C=O). Zhluktov and Abe [49] already introduced this distinction between at least two different types of adsorption into a kinetic model. This is also justified by several studies demonstrating the heterogeneity of the active surface sites in carbon materials. Lussow *et al.* [51] determined the active site density on Graphon samples with O<sub>2</sub> chemisorption and found that, above 400°C, the oxygen saturation on the surface sharply increases, suggesting the presence of at least two types of active sites. Later on, Ahmed *et al.* [52] developed a kinetic model to describe the O<sub>2</sub> gasification of pyrolytic carbon, at low pressure (100 Pa) and in a narrow temperature range (748 – 898 K). The proposed mechanism involved the distinction between two types of active surface sites, and unveiled the importance of such distinction for an accurate description of CO<sub>2</sub> desorption. More recently, density functional theory (DFT) calculations demonstrated that the description of the heterogeneity of the surface of carbons through at least two types of active sites is needed to explain the desorption of CO<sub>2</sub> [53,54].

As suggested by Prata [55], we defined the distribution between sites giving mobile and immobile chemisorption to be 30% and 70%, respectively. The activation energy for the CO desorption stimulated by collisions with gas molecules (or atoms) is increased to 6000 K in order to match the experimental trends with our 0D kinetic model. For the same reason, we have lowered the pre-exponential factors to unity. The stimulated CO desorption is modeled as an Eley-Rideal reaction, where the pre-exponential factors typically take values between 0 and 1. Moreover, Prata [47] determined the activation energy and pre-exponential factors by fitting with molecular beam experiments, under the assumptions that i) the desorption products are immediately removed from the surface and ii) the hyperthermal O and O<sub>2</sub> sent to the surface accommodate to the surface temperature. However, products may also interact with the surface

and the O/O<sub>2</sub> beam might not be in equilibrium with the surface temperature, also mentioned by the author [47]. The choice of a larger activation energy is also supported by the value proposed by Yang and Yang [56] for the spontaneous CO desorption (see Table 3), by the values estimated by Tremblay *et al.* [57] and by the values computed by Montoya *et al.* [58]. Following the same reasoning, we increased the activation energy also for the CO<sub>2</sub> desorption, by choosing a value proposed by Zhlukov and Abe [49] in their model for carbon oxidation. The experimental evidences from Panerai *et al.* [41] corroborate our choice. In particular, the authors show that CO<sub>2</sub> is produced only at temperature higher than 700 K under O<sub>2</sub> atmosphere, whereas the use of the energy barrier proposed by Prata would lead to overestimation of CO<sub>2</sub> for lower temperatures. Moreover, we performed a thermogravimetric analysis (TGA) (see Fig. S3 in SI) for charcoal 1, and the results are in good agreement with Panerai *et al.* i.e. CO<sub>2</sub> desorption onsets only above 700 K. Finally, it is worth to remark that the activation energy of the surface reactions varies with the structure of the carbon material, the oxidation degree of the surface and the presence of catalytic impurities.

Furthermore, to study the reactions occurring between CO<sub>2</sub> and the carbon active sites, we also implement the heterogeneous Boudouard reaction set proposed by Yang and Yang [56], reported in Table 3. The rate constants for the elementary steps were determined in a temperature range of 873-1173 K for graphite. In order to integrate it with the above carbon oxidation set, we assumed that the dissociation of CO<sub>2</sub> leads to formation of 30% mobile and 70% immobile oxygen chemisorption, as for atomic oxygen. The existence of at least two different types of oxygen adsorption is also documented for CO<sub>2</sub>. For instance, Yang and Yang [56] found out that, after CO<sub>2</sub> gasification of graphite, the bond strength of the oxygen complexes formed on the monolayer edges is about 9 kcal mol<sup>-1</sup> stronger than the complexes formed on the multilayer edges, and that they have an average bond character of two-thirds. Later, Calo and Perkins [51] stressed the need of accounting for the energetic heterogeneity of carbon surfaces in the kinetic analysis of the CO<sub>2</sub> gasification.

Table 3. Heterogeneous Boudouard reactions and their rate coefficients taken from Yang & Yang [56].

Reaction	Rate constant	Units
CO(g) + C(s)-O ⇌ CO <sub>2</sub> (g) + C(s) (Forward Boudouard)		[cm <sup>3</sup> s <sup>-1</sup> ]
CO <sub>2</sub> (g) + C(s) ⇌ CO(g) + C(s)-O (Reverse Boudouard)		[cm <sup>3</sup> s <sup>-1</sup> ]
C(s)-O ⇌ CO(g) (CO spontaneous desorption)		[s <sup>-1</sup> ]



Where  $R$  is the ideal gas constant [L atm K<sup>-1</sup> mol<sup>-1</sup>].

### 3.2. Experimental input parameters for the model validation

As mentioned in the Introduction, we have chosen to validate our model with the gasification experiments presented by Panerai *et al.* [41], separately under O<sub>2</sub> and CO<sub>2</sub> atmosphere. Indeed, their experimental setup has a simple design. It can be approximated as a plug flow reactor and allows to isolate the effect of O<sub>2</sub> and CO<sub>2</sub> in the oxidation and consumption of solid carbon. Moreover, the absence of a plasma further reduces the complexity of the process, and therefore the number of experimental uncertainties, and it will enable us to investigate in a second stage the effect of plasma in the gasification mechanism, establishing solid foundations for future model developments.

The experiments carried out by Panerai *et al.* [41] provide a set of experimental data which can be implemented into our 0D kinetic model with relative ease. A cylindrical glass tube is placed inside a furnace, within which the temperature can be assumed homogeneous and constant. The carbon bed is fitted inside the glass tube, approximately at the center of the furnace. The feed gas, either pure O<sub>2</sub>, CO<sub>2</sub> or CO, flows through the tube and reaches the carbon bed heated by the furnace. The products are then analyzed downstream by Residual Gas Analysis (RGA) mass spectrometry. This simple experimental configuration can be approximated to a plug flow reactor under a limited number of assumptions, the most important being that the fluid is perfectly mixed in the direction perpendicular to the axis. In addition, the high-temperature oxidation experiments were performed using FiberForm, a carbon fiber material which is thoroughly characterized [59–61] and therefore an excellent candidate for modelling purposes. Thus, this experimental set of data represents a good benchmark for the validation of our 0D kinetic model. The parameters taken by the experimental work of Panerai [41] and used in our modelling study are listed in Table 4. Note that for the validation step with their experiments [41], the temperature is assumed constant and homogeneous throughout the reactor tube in the model. This assumption is needed since we had no information about the actual temperature at the carbon bed. We know from our experiments that the temperature increases locally where oxidation reactions take place, due to their exothermic nature. However, the use of a furnace, as in Panerai *et al.* [41], may help to maintain the temperature uniform in the carbon bed, and we believe that this supports our assumption. In our experiments, on the other hand, the carbon bed is partially heated by the plasma, and also locally heated by oxidation reactions. Therefore, we measured the temperature variations in the carbon bed, as well as without, with the aim of linking our modelling results, for fixed gas temperatures, to our experiments.

Table 4. Parameters used for the 0D simulations, taken from Panerai *et al.* [41]

Test	Feed gas	T [K]	P [Pa]	C <sub>0</sub> mass [g]	Carbon bed length [mm]	mass flow rate [g s <sup>-1</sup> ]
O <sub>2</sub> _A	O <sub>2</sub>	518	2172	1.366	20	2.36
O <sub>2</sub> _E	O <sub>2</sub>	1086	3668	1.357	20	2.34
O <sub>2</sub> _H	O <sub>2</sub>	1502	6180	1.372	20	2.34
O <sub>2</sub> _H <sub>600</sub>	O <sub>2</sub>	1502	1900	0.372	7.18	2.34
CO <sub>2</sub> _C	CO <sub>2</sub>	983	2674	1.350	20	2.31
CO <sub>2</sub> _H	CO <sub>2</sub>	1413	4176	1.330	20	2.31
CO_C	CO	1508	3954	1.383	20	2.06

The notation for each individual test listed in Table 4 is taken from Panerai *et al.* [41]. The notation indicates the feed gas (O<sub>2</sub>, CO<sub>2</sub> or CO), while the letters A, E, H and C were arbitrarily chosen by Panerai *et al.* to enumerate the tests, but in fact they correspond to different temperatures (see Table 4). Note that only the tests for which the product concentrations were recorded over time and provided from the experiments have been used in this study. For test O<sub>2</sub>\_H, we performed an additional simulation, named O<sub>2</sub>\_H<sub>600</sub>, with pressure, carbon mass and carbon bed length after 10 minutes of treatment. For each single test, the temperature is assumed constant and homogenous throughout the reactor tube inside the furnace. The experiments were carried out at controlled mass flow rate, with variable pressure. The initial mass of each carbon bed sample was weighted, allowing for a more accurate calculation of the absolute total surface area (TSA), in square meters, for each individual test. We estimated a specific surface area of 0.16 m<sup>2</sup>/g for FiberForm, following the calculations presented by Gusarov [62]. This estimation is in the same order of magnitude of other carbon fibers [63,64]. The TSA is a useful parameter to estimate the density of active sites  $C_{surf}$  (cm<sup>-3</sup>), as described in formula 10:

$$(10)$$

Where  $b$  is a fitting parameter,  $B$  is the active site density over the surface in mole m<sup>-2</sup>,  $N_A$  is the Avogadro number and  $V_{bed}$  is the volume of the carbon bed in cubic meters. The choice of introducing the parameter  $b$  to calculate the active site density  $C_{surf}$  is justified by the influence of the experimental pressure on the reactivity of the carbon materials. Ismail [63] observed that at pressures above 2.67 kPa, a new type of active sites is activated. In molecular-beam studies, the pressure is typically near vacuum. Therefore, it is reasonable to assume that at higher pressures, such as in the experiments by Panerai *et al.*, the density of active sites is larger. This is consistent with the fact that without a fitting parameter to enhance the reactivity, the simulations predict a negligible effect of the carbon bed, in contrast

with the experimental observations. We decided to keep  $b$  fixed at 30, as it provided the best agreement with the experiments. We do not expect  $b$  to vary significantly between one test and another, as the pressure is maintained within the same order of magnitude throughout the entire experimental study. We would like to point out that the chemistry set and the model developed for this study are only suitable to quantitatively simulate the performance of the gasification process under the conditions tested in the experiments by Panerai *et al.* [41]. With the aim of describing a different system (e.g. with different carbon materials or operational pressure), a tuning of the kinetic model may be required. Nevertheless, the model can still provide insights into the underlying mechanisms, even when the experimental conditions vary.

## 4. Results and Discussion

### 4.1. Performance comparison: with and without carbon bed

Figure 3 presents the maximum CO<sub>2</sub> conversion, and the corresponding energy efficiency and energy cost, without carbon bed (benchmark) and for two different carbon materials with different particle size, namely active charcoal 1 and 2 (see previous section). The obtained maximum CO and O<sub>2</sub> concentrations are also depicted in Figure 3.

Figure 3. Conversion, energy efficiency, energy cost, and CO and O<sub>2</sub> concentrations (obtained at the maximum conversion; see below), without carbon bed (benchmark), and with carbon bed (charcoal 1 and charcoal 2). 10 L.min<sup>-1</sup> CO<sub>2</sub>. The SEI was about 3.2 kJ L<sup>-1</sup> in all cases.

It is known that the physicochemical properties of the carbon material and the particle size can seriously affect the carbon reactivity towards CO<sub>2</sub> during gasification [65,66]. More specifically, the concentration of active sites where the heterogeneous reactions between CO<sub>2</sub>, O/O<sub>2</sub> (from gas) and carbon (from solid) occur is a critical parameter. Indeed, we observe a difference, with charcoal 1 producing slightly better results, but also somewhat larger error bars. This could be due to the larger pellet size, inducing more inhomogeneity in the bed. Nevertheless, we believe the better performance of charcoal 1 is attributed to a better gas and heat transfer. Indeed, larger particles leave more open space, which yields better convective heat transfer. As a result, when we measure the pressure upstream the carbon bed, the overpressure is less than 550 Pa (= resolution of our measurements) with charcoal 1 and ca. 2800 Pa with charcoal 2. By contrast, charcoal 1, with larger pellet size, may limit the intra- and inter-particle diffusion, with a bigger effect on the former, affecting the reactivity of charcoal towards CO<sub>2</sub> [67]. However, because charcoal 1 and 2 have slightly different characteristics besides the particle size (e.g. charcoal 1 is steam activated, charcoal 2 is untreated), it is not

possible to exactly estimate the effect of the mass transfer limitations. Indeed, charcoal 1, despite the larger particle size, provides higher CO<sub>2</sub> conversion and CO yield. We would like to address this question in our future work, where we will compare the performance of different pellet sizes, but of the same exact material, if available.

Nevertheless, whatever the type of charcoal (1 or 2), the conversion is significantly enhanced with the carbon bed, almost by a factor of two (from  $7.6 \pm 0.1$  to  $12.6 \pm 2.0$  % and  $11.3 \pm 1.2$  % for charcoal 1 and 2, respectively), for the same SEI (about  $3.2 \text{ kJ.L}^{-1}$ ). Consequently, the energy efficiency is increased from  $27.9 \pm 0.1$  % to  $45.4 \pm 6.8$  % and  $40.4 \pm 2.5$  % for charcoal 1 and 2, respectively, whereas the energy cost is much lower (from  $41.9 \pm 0.2 \text{ kJ.L}^{-1}$  for the benchmark to  $25.4 \pm 4.2 \text{ kJ.L}^{-1}$  and  $28.5 \pm 2.0 \text{ kJ.L}^{-1}$  for charcoal 1 and 2, respectively). The exact contribution of the RBR in the chemical process is not known, and, as mentioned in section 2.3, we expect it to play a minor role at the conditions under study (i.e., temperature in the carbon bed is only at the limit for the RBR to occur), so we calculated the energy efficiency based on for pure CO<sub>2</sub> splitting. This must however be kept in mind for the values obtained with the carbon bed. Finally, Figure 3 also shows that the CO concentration is about three times higher upon addition of the carbon bed, while the amount of O<sub>2</sub> is negligible when the carbon bed is present.

Therefore, adding a carbon bed not only favourably improves the CO<sub>2</sub> conversion and increases the CO concentration, but also gives much better energy efficiency and a much lower energy cost. In addition, the exhaust can be kept free of oxygen, which is very beneficial, as it avoids separation costs of CO from O<sub>2</sub>. Indeed, besides removal and recycling of unconverted CO<sub>2</sub>, CO purification is a technical challenge in case of scaled-up facilities, and thus an expensive process [37]. A CO<sub>2</sub>/CO mixture obtained in the presence of a charcoal bed, free of O<sub>2</sub>, could be directly recycled, by recirculating the gas in the plasma reactor, increasing the CO<sub>2</sub> conversion and eventually (ideally) leading to a pure CO stream. Note that recycling the exhaust in the plasma reactor again would reduce the overall energy efficiency, because energy is again needed for the second pass through the plasma. In real-life application, however, especially featuring near-zero cost renewable energy sources, there will be a trade-off between CAPEX (more reactors) and OPEX (recycling, hence more energy needed).

A similar improvement of the CO<sub>2</sub> conversion in the presence of a carbon bed was obtained with an atmospheric non-thermal plasma system studied by Huang *et al.* [34] (conversion up to 21.3 % with carbon bed), but with a rather low associated energy efficiency (24.0 %) due to a relatively high SEI ( $\approx 7 \text{ kJ/L}$ ) compared with our conditions (where the SEI is  $3.2 \text{ kJ/L}$ ). In a thermal plasma, the CO<sub>2</sub> conversion was even more increased (up to 95 %) at a very high energy efficiency (70 %), as studied by Li *et al.* [32]. However, these experiments were performed in CO<sub>2</sub>/Ar mixtures, and Ar helps to enhance the CO<sub>2</sub> conversion and energy efficiency [8], but in reality, Ar also consumes part of the plasma energy, which was not accounted for when calculating both the conversion and energy efficiency. For a fair comparison, the fraction of CO<sub>2</sub> in the mixture should be accounted for [20,8]. Therefore, we cannot compare the

absolute values. Moreover, because of the thermal plasma, the temperature was considerably higher (more than 1000 °C at 6 cm from the initial carbon surface) and therefore more beneficial for the RBR. A very high power (up to 16 kW) was necessary to drive this thermal plasma, which is far from our operating conditions (power around 0.5 kW). The authors proposed the following mechanism: CO<sub>2</sub> is first decomposed in a CO/O/O<sub>2</sub> mixture that reaches the carbon bed with a high temperature, favouring carbon oxidation by oxygen atoms and molecules; Second, the unconverted CO<sub>2</sub> is able to react with the carbon bed via the RBR thanks to the elevated temperature from exothermic oxidation reactions [32].

In the next sections, we present the measured temperature profile after the plasma reactor, as well as the time-evolution of the CO<sub>2</sub>, CO and O<sub>2</sub> concentrations, to explain the influence of the carbon bed on the CO<sub>2</sub> chemistry after the plasma in our conditions. Furthermore, we will also present modelling results, to validate our hypotheses.

#### **4.2. Temperature profile after the plasma reactor, without carbon bed**

We measured the temperature profile after the plasma reactor, without carbon bed, to gain more insight in the chemical reactivity of the carbon towards CO<sub>2</sub>, CO, O and O<sub>2</sub> [41] (also needed to interpret the modelling results presented in section 4.6 below) and to determine the most suitable position of the carbon bed in the post-plasma reactor tube. The results are presented in Figure 4 (red curve). Note that the post-plasma reactor tube was designed so that the temperature could be measured over the entire length (i.e. up to 255 mm), if necessary. However, we were most interested in measuring the temperature close to the reactor outlet, so we only measured up to 140 mm, because at further distances, the temperature is not so elevated anymore (see Figure 4).

Figure 4. Measured temperature profile in the post-plasma region without carbon bed (basket removed), with two different power supplies. Flow rate: 10 L.min<sup>-1</sup> CO<sub>2</sub>, SEI = 2.9 kJ. L<sup>-1</sup>.

Note that the error bars, based on three independent measurements, are too small to be visible. Moreover, when the carbon bed is present, it starts at 0 mm (right at the reactor outlet) and extends till 60 mm (see vertical dashed line). In absence of the carbon bed, the temperature profile exhibits an exponential decrease with increasing distance from the reactor outlet (red curve). At 15 mm distance, the temperature reaches about 850 K and it drops to about 450 K at 95 mm distance. Note that for positions < 15 mm, the thermocouple tip was molten, as it was most likely in direct contact with the arc extending out of the plasma reactor, which made the measurements not possible. Based on previous modelling results, the arc temperature in the GAP is around 3000 K [44], so we can expect the temperature to be much higher than 850 K closer to the reactor outlet. Earlier, we had performed similar measurements for the same setup but with another power supply (APS; Advanced Plasma Solutions). However, the latter power supply later got broken, so

it could not be used for our plasma conversion experiments. Nevertheless, we plot these temperature measurements in the same figure (black curve). They show a similar profile, and because the plasma arc behaviour was a bit different due to a different operational mode (attributed to the power supply), measurements closer to the reactor outlet were possible in this case, without melting the thermocouple tip. We could measure up to 1300 K at 4 mm distance from the reactor outlet. Although the temperature profile is slightly different for a distance  $> 35$  mm, the trend indicates a very similar behaviour for positions  $< 25$  mm and therefore similar temperatures are expected close to the reactor outlet with the actual power source (red curve). Thus, positioning the carbon bed as close as possible to the reactor outlet (hence: to the plasma) allows the carbon bed not only to be in contact with the reactive O atoms from the plasma (providing quenching, so that they do not contribute to the back-reactions; see Introduction), but also to take benefit from the high temperature to enhance possible reactions between the exhaust gas and the solid carbon. This temperature profile will be used to explain the underlying chemical reactions, described in the model, in section 4.6 below.

#### **4.3. Time-evolution of CO<sub>2</sub>, CO and O<sub>2</sub> concentrations, and associate CO<sub>2</sub> conversion**

To better understand the chemical reactions occurring at the carbon bed and explain the very good results from Figure 3, we plot in Figure 5 the concentrations of CO<sub>2</sub>, CO and O<sub>2</sub> in the exhaust gas mixture as a function of time during plasma exposure, both without and with carbon bed (Figure 5A and 5B) by using NDIR/O<sub>2</sub> optical sensors, and we also compare with GC measurements, to ensure a good accuracy of the optical sensors (Figure 5C). Note, however, that the GC measurements only allowed a few time points; hence the advantage of the optical sensors. We only present the results for charcoal 1, but the data for charcoal 2 were very similar.

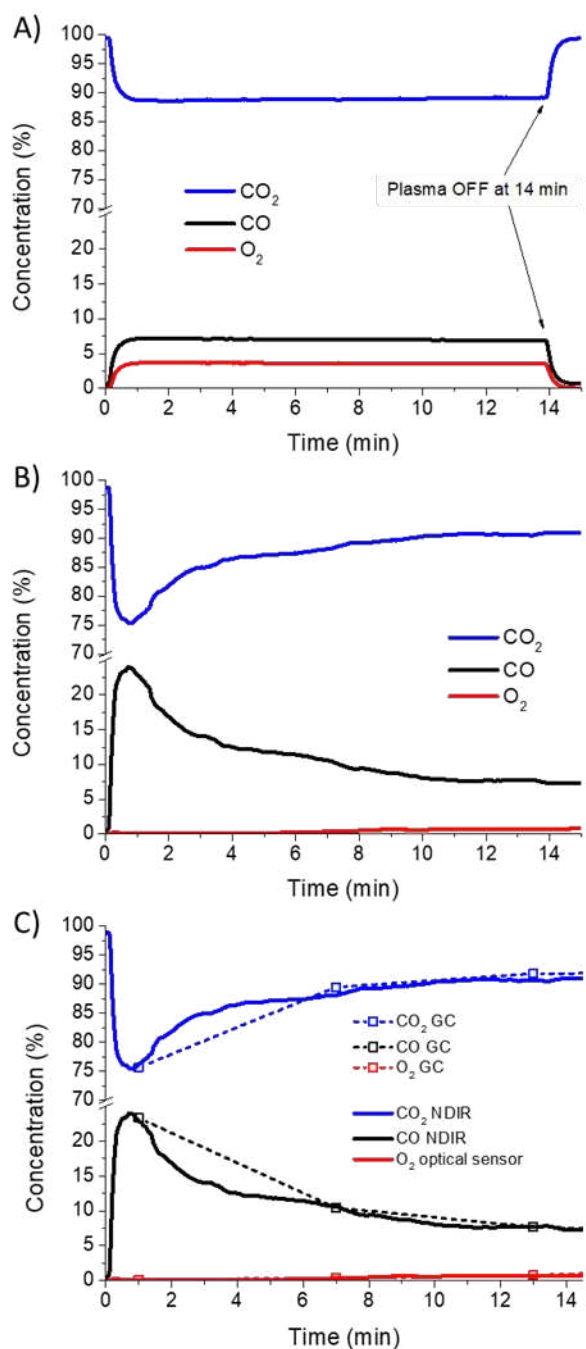


Figure 5. CO<sub>2</sub>, CO and O<sub>2</sub> concentrations measured in real time, without carbon bed (A) and with carbon bed filled with charcoal 1 (B); C. Comparison of the optical sensors with GC measurements which only allow a few time points. Charcoal 1, 10 L.min<sup>-1</sup> CO<sub>2</sub>, SEI = 3.2 kJ.L<sup>-1</sup>. The plasma is turned ON at time 0.

Without carbon bed (Figure 5A), when the plasma is turned ON, the CO<sub>2</sub> concentration immediately drops to about 88%, whereas the CO and O<sub>2</sub> concentrations rise to 7.2 % and 3.6 %, respectively. In less than one minute, the three concentrations stabilize and stay constant over time, meaning that the plasma reaches an equilibrium, in line with previous studies with this plasma reactor [39,43]. Once the plasma is turned OFF, i.e., at 14 min, the chemical

reactions stop and the concentrations return to their original values. The only reaction occurring here is CO<sub>2</sub> splitting, producing CO and O<sub>2</sub>, as described in Equation 1 in the Introduction.

Upon addition of a carbon bed (Figure 5B), the concentrations feature a quite different evolution over time. The CO<sub>2</sub> concentration immediately drops after plasma ignition and reaches a minimum value (ca. 75 %) within 30-40 sec, and then gradually increases to ca. 90 % at 14 min. The CO concentration reaches up to 24 % when the CO<sub>2</sub> concentration is minimal, and then decreases again, similarly to the CO<sub>2</sub> increase. In contrast, the O<sub>2</sub> concentration depicts a very small transient rise right after plasma ignition ( $\approx 0.2$  %, see Figure S8) before dropping to a negligible amount for about 5 minutes, followed by a very slow increase, but it stays below 0.8 % as final value. A similar evolution was observed by Huang *et al.* with an atmospheric non-thermal plasmatron [34]. Therefore, the comparison between (A) and (B) shows that the carbon bed is deactivated after some time, for the production of CO (which relaxes to the benchmark value) but not for the O<sub>2</sub> consumption. The underlying mechanisms will be discussed later in sections 4.5 and 4.6.

To verify the accuracy of our NDIR and O<sub>2</sub> optical sensor measurements, we compared them with GC analysis, performed at the same time in parallel. GC is a very common technique for analysing gas mixtures and known to be very efficient and reliable; however, in the context of these experiments, on-time measurement is more useful to understand the complex chemistry. The results are presented in Figure 5C and indicate a very good agreement between both techniques. Therefore, we can consider the on-time data reliable to calculate the conversion and the performance of the carbon bed.

From the time-profile of the CO<sub>2</sub> concentration (Figure 5), we calculated the CO<sub>2</sub> conversion (eq. 4 and 5) for both the benchmark and the carbon bed addition, and the results are plotted in Figure 6. In the first 1-2 minutes, the conversion upon carbon bed addition is much higher than without carbon bed, but it drops to lower values after ca. 3 minutes. In the next section, we discuss the results of the characterization study of the charcoals, before and after the gasification reaction.

Figure 6. CO<sub>2</sub> conversion as a function of time without (dash line) and with (solid line) carbon bed. Charcoal 1, 10 L.min<sup>-1</sup> CO<sub>2</sub>, SEI = 3.2 kJ.L<sup>-1</sup>.

#### 4.4. Characterization of charcoal before and after the gasification reactions

The gasification of solid carbon is governed by interdependent factors such as the micro- and macrostructure of the material, the total and the active surface area, the degree of oxidation, the presence of catalytic impurities and the gas-



phase composition. Any modification of one of these factors may alter the others. Therefore, the study of the underlying mechanisms for the gasification process, and their variations with time, cannot be separated from the screening of the modifications occurring during the reaction. For this purpose, we analysed the alterations of the surface exposed to the plasma-treated gas mixture, using SEM, N<sub>2</sub>-BET and TGA-MS. The SEM images were collected for charcoal 1 as received and after 45 s and 7 minutes of reaction (see Figure S2 in SI). From the images, we could not identify any visible morphology change during the gasification reaction, except for the formation and deposition of ashes over the surface, which look more intense after 45 s rather than after 7 minutes of reaction. The BET measurements were performed on charcoal 1 and 2, as received, and after the gasification reaction for charcoal 1. The results are given in Table 5.

Table 5. BET measurements of the surface area.

Sample	BET surface area [m <sup>2</sup> g <sup>-1</sup> ]
Charcoal 1	705 ± 71
Charcoal 2	703 ± 70
Charcoal 1, after 45 s, top layer	767 ± 77
Charcoal 1, after 45 s, bottom layer	732 ± 73
Charcoal, after 7 minutes	787 ± 79

The BET measurements reveal that charcoal 1 and 2 have the same initial surface area. For this reason, we decided to perform the measurements after the reaction only for charcoal 1. After 45 s, the CO<sub>2</sub> conversion spikes (see Figure 6) and the temperature is higher than 1300 K at 15 mm in the carbon bed, in the top layer, and still lower than 500 K at 35 mm, in the bottom layer (see Figure 7, below). Therefore, it is reasonable to deduce that the gasification reactions are mainly occurring in the top layer of the bed. However, the surface area is barely affected, with a bigger effect on the top layer, most likely because of the desorption of volatile species (e.g. water) from the surface during the first seconds of reaction. After 7 minutes, the temperature in the top and bottom layer is nearly the same (see Figure 7). At this point, Figure 6 shows that the carbon bed is deactivated and the CO<sub>2</sub> conversion is lower than the benchmark value. Regardless of this, the surface area is further increased compared to 45 s. In view of the above, we cannot clearly link drop in performance of the carbon bed with a change in morphology or surface area. To investigate the presence of adsorbed species and thermolabile functional groups at the charcoal surface, before and after the gasification reaction, we carried out a TGA-MS study. The analysis highlighted that water is the main species desorbed by charcoal, already at low temperature (see Figure S4 in SI). This is an indication that water is mainly adsorbed over the surface and not coming from the decomposition of surface functional groups. Only at about 850 K, CO<sub>2</sub>, CO and H<sub>2</sub> are also detected. We would like to point out that the analysis is not quantitative, and we need to be careful when comparing different products in terms of magnitude, because the mass spectrometer was not calibrated. However, at this point, H<sub>2</sub>O

desorption drops, and we hypothesize that a fraction of the other species detected are products of the reaction between water and charcoal, also called steam gasification [68,69]:

, With (11)

The presence of CO<sub>2</sub> could be explained by either the water-gas shift reaction [69]:

, With (12)

or by the decomposition of oxygen complexes or surface functional groups i.e. carboxyl groups [70], naturally found in charcoals. However, the TGA-MS of charcoal 1, after 45 s and 7 minutes of reaction (see Figure S5 and S6, respectively in SI), shows that water is still the main species desorbed from the surface, despite charcoal was certainly exposed to high temperatures during the gasification reactions. Such an observation indicates that water is probably re-adsorbed from the moisture in the atmosphere after the reaction, as charcoal is a hygroscopic material [71]. For this reason, it is not possible to draw clear conclusions from this analysis. However, the weight loss during the TGA (see Figure S7 in SI) shows that the charcoal tends to release less gaseous products with increasing gasification time, indicating that the surface may undergo a physico-chemical transformation that reduces the hygroscopicity of charcoal and/or modifies the nature or the amount of complexes and functional groups at the surface, favouring more stable interactions. With the results presented above, we hypothesize the underlying mechanisms in the next section.

#### 4.5. Hypothesis of the underlying mechanisms

Based on the conversion and concentrations as a function of time, plotted in Figures 5 and 6, we hypothesize that the following mechanisms take place:

1/ First, the conversion increases abruptly up to 14 % (corresponding to the minimal CO<sub>2</sub> concentration observed in Figure 5B). We can reasonably assume that, when the converted mixture (containing CO<sub>2</sub>, CO and O/O<sub>2</sub>) is flowing through the carbon bed, O and/or O<sub>2</sub> are immediately adsorbed (either chemically or physically) on the carbon surface, as depicted in Figure 5B and Figure S8 in SI. Hence, recombination reactions (CO + O/O<sub>2</sub> forming again CO<sub>2</sub>) are suppressed and the net conversion increases, producing at the same time more CO compared with the benchmark (cf. Figure 5A,B). The most likely mechanism occurring here is the partial oxidation of carbon by O/O<sub>2</sub>, following equations 13 and 14 [41,47,72]:

(13a)

(13b)

(14)

With C(s) a solid carbon active site. In Equations (13a,b), O and O<sub>2</sub> are immediately adsorbed by the carbon bed, followed by the release of a CO molecule promoted by collisions with gas molecules and high temperature (Equation 14).

Note that for CO<sub>2</sub> splitting without carbon bed, the CO<sub>2</sub> conversion is usually equal to the CO concentration in the exhaust. Indeed, for the benchmark, both CO<sub>2</sub> conversion and CO concentration are about 7 – 7.5 % in this case (Figure 5A and Figure 6). With carbon bed, the maximum conversion is 14 % (Figure 6), whereas the associated CO concentration is 1.5 times higher, i.e., 22 %. Therefore, we can reasonably assume that part of the measured CO is released from the carbon surface, as described in Equation 14, in addition to CO coming from initial CO<sub>2</sub> splitting, which is most likely unreactive toward solid carbon [41]. A second hypothesis is that the RBR takes place as well (Equation 2 in the Introduction), but only if high enough temperature can be achieved (above ca. 973 K [65]) to activate the reaction towards the formation of CO. This will be further discussed in section 4.6 below.

2/ After this peak, the conversion decreases until reaching the benchmark value in around 3 minutes, whereas the CO concentration decreases and the O<sub>2</sub> concentration starts rising. Even more, from then on, the conversion continues dropping until being about 2 % lower than the benchmark value, meaning that the positive effect previously observed does not last over time. We hypothesize that the carbon surface reaches saturation of oxygen: gas-phase O/O<sub>2</sub> is still being consumed by the remaining pellets that are not yet saturated (as seen in Figure 5B and Figure S9) but it now leads to full oxidation and the release of CO<sub>2</sub> molecules (Equation 15). The role of the formation of oxygen complexes at the surface, most likely epoxy and peroxy complexes, on the CO<sub>2</sub> evolution during the carbon oxidation reactions, is also underlined by DFT calculations [73]. Moreover, the forward Boudouard reaction takes place (as demonstrated by our computer simulations; see section 4.6 below), explaining why the performance in terms of conversion becomes lower than the benchmark.

(15a)

(15b)

Moreover, as the oxidation reactions (sum of the elementary reactions 13 and 15) are exothermic [41,74,75], heat will be released and thus we expect an increase of the carbon bed temperature compared to the benchmark. In order to check this, we measured the temperature in the carbon bed (cf. Figure 1 above) and compared it with the benchmark (in this case, the temperature is also measured in the basket, but free of carbon). The results are presented in Figure 7, measured at 15 mm from the reactor outlet (dark blue line).

Figure 7. Measured temperature at 15 mm and 35 mm from the reactor outlet, with carbon bed (dark and light blue lines, respectively), and without carbon bed (black line). Charcoal 1, 10 L.min<sup>-1</sup> CO<sub>2</sub>, SEI = 3.2 kJ.L<sup>-1</sup>.

The temperature in the carbon bed reaches a maximum almost immediately after plasma ignition (ca. 1700 K), then decreases to finally stabilize around 1200 K after 2 minutes. Note that the temperature at 35 mm from the reactor outlet (light blue line in Figure 7) is lower than at 15 mm during the first 4 minutes. This shows that the temperature profile is not uniform along the carbon bed and depends on the distance from the plasma. Moreover, we can assume that the carbon pellets at the end section of the basket are not yet saturated, as O atoms and O<sub>2</sub> are being consumed by the top layer. However, after 4 minutes the temperature at 35 mm increases and becomes higher than at 15 mm. It strengthens our hypothesis of full oxidation occurring at a later stage on the pellets placed further away from the anode exit (35 mm vs 15 mm) when they are saturated with oxygen (Equation 15).

As mentioned above, we believe that the initial rise in temperature at 15 mm, observed in Figure 7, is due to exothermic reactions, most likely partial carbon oxidation (Equations 13-14) [76]. When the temperature is around 1200 K, CO<sub>2</sub> is most likely released from the surface, at the expense of CO [41], and this is what we actually observe in Figure 5B.

Moreover, it is very likely that the RBR occurs at such high temperature (1700 K) [32,34]. This is a highly endothermic reaction (see eq. 2 in the Introduction), so we can expect the temperature to be even higher than the measured one, but probably in a short period of time. Its contribution is however not straightforward to evaluate compared with carbon oxidation, which is more obvious from our experimental results. In any case, the presence of the carbon bed strongly influences the temperature, especially during the first minutes. Furthermore, the presence of the carbon bed might also affect the flow dynamics (physical effect), and consequently, this may affect the temperature. Hence, to discriminate between this physical effect and the chemical effects, we have replaced the carbon bed with an unreactive material (i.e., ceramic beads) that can withstand high temperatures. The temperature in the “dummy bed” did not exceed 1000 K, with associated CO<sub>2</sub> conversion and CO/O<sub>2</sub> concentrations similar to the benchmark values.

Therefore, the main reason for the elevated temperature with the carbon bed is indeed most likely due to the exothermic reactions (13) and (15), as previously explained.

In comparison, the temperature in the basket without carbon (black line in Figure 7) is lower and rather constant in the range of 1000 - 1050 K. This temperature is higher than at the same position without basket (about 850 K; see Figure 4 above). This could be explained by the limited gas circulation inside the basket, its thick walls are heated up and they keep on releasing heat to the gas during the process.

In addition, the carbon bed may also represent a physical constraint to the flow, increasing the pressure upstream and causing a pressure drop throughout the bed. Panerai *et al.* [41] reported a pressure drop of up to ca. 90% under their conditions. Such a drop can be ascribed to the use of a roots pump to evacuate the system downstream their carbon bed. However, they did not discuss the effects of the pressure drop to the performance of their reactor. In our experiments, we could only estimate the drop by measuring the overpressure built upstream the carbon bed and assuming that the pressure downstream the bed is equal to atmospheric pressure. This is a good approximation since the exhaust flow is evacuated to open air, under the fume hood, without any pump. From our pressure measurements, we estimated the pressure drop to be lower than 0.4% for charcoal 1 and ca. 2% for charcoal 2. Therefore, we do not expect the pressure drop to play any significant role in the performance of the process under our operational conditions.

Finally, as shown in Figure 1, the silo should provide fresh carbon once depleted in the basket and thus prolong the positive effect observed during the first minutes. Hence, the question arises whether the silo is not working properly. However, in another experiment in similar conditions (see Figure S9 in SI), we observed a sudden rise in temperature of about 100 K after ca. 10 minutes, followed again by a decrease. At the same time, the O<sub>2</sub> concentration drops to zero again, but for a very short period. This phenomenon is most likely due to fresh carbon supplied by the silo in the basket, leading to a drop in O<sub>2</sub> concentration and a small bump in CO<sub>2</sub> and CO concentration profiles (see Figure S9), following equations 9 and 10. However, the amount of fresh carbon seems insufficient to quench all the O/O<sub>2</sub>, as observed in Figure S9 (the O<sub>2</sub> concentration rises again almost immediately, see inset figure), and therefore the positive effect remains limited. In any case, the temperature in the carbon bed seems very much linked to the CO<sub>2</sub>, CO and O<sub>2</sub> behaviour in the mixture, but the cause and effect is not straightforward to understand and requires more in-depth analysis based on chemical kinetics modelling. Therefore, in the next section, we provide results of our model for the carbon gasification with different feed gases and we link the outcome to our experimental observations. This helps us indeed to better understand our experimental results.

#### **4.6. Testing the hypothesis by means of modelling**

Aiming to validate the set of reactions included in our model, we simulated the experimental tests listed in Table 4 in section 3.2 above, with the corresponding input parameters. The simulated product compositions, compared against the experimental values of Panerai *et al.* [41], are depicted in Figure 8. Note that the product concentrations are taken at steady-state, which is reached within 200 s of treatment at all the conditions tested, except for O<sub>2</sub>\_H<sub>600</sub>, for which the comparison refers to the product concentrations after 600 s of treatment.

Figure 8. Comparison between experimental (solid) [41] and simulated (diagonal pattern) product concentrations (see section 3.2 and Table 4 for the notation and the experimental conditions). The uncertainty on the concentration of the oxidation products was reported to be  $\pm 12\%$  [41].

Figure 8 shows that the model is able to capture the experimental trends and predict the product composition reasonably well. In particular, both our simulations and the experiments highlight no reactivity of solid carbon towards O<sub>2</sub> at 518 K (O<sub>2</sub>\_A), i.e., the only “product” is unreacted feed gas (O<sub>2</sub>). Furthermore, they also agree on the total consumption of O<sub>2</sub> at higher temperature i.e. 1086 K (O<sub>2</sub>\_E) and 1502 K (O<sub>2</sub>\_H), producing 20-25 % CO and 75-80 % CO<sub>2</sub> at 1086 K, and pure CO at 1502 K. The reaction analysis for O<sub>2</sub>\_E and O<sub>2</sub>\_H (see Figure S10 and S11 in SI, respectively) indicates that O<sub>2</sub> promptly chemisorbs at the carbon surface, forming oxygen complexes. However, CO desorption is kinetically limited at 1086 K, therefore the oxygen complexes accumulate at the surface and can only undergo total oxidation (low activation energy), releasing CO<sub>2</sub> and consuming all the O<sub>2</sub>. As a result, CO<sub>2</sub> is the main oxidation product in this case (O<sub>2</sub>\_E).

At 1502 K, CO desorption is kinetically favoured and competes with C(s)-O oxidation ( $\text{O}_2(\text{g}) + \text{C}(\text{s})-\text{O} \rightarrow \text{CO}_2(\text{g}) + \text{O}(\text{g})$ ). Interestingly, the Boudouard equilibrium favours the CO<sub>2</sub> production until 1 cm in the carbon bed (see Figure S11 in SI). At that point, most of the active sites are free (see Figure 9), as CO has been desorbed, and the RBR can proceed and convert CO<sub>2</sub> back to CO. As a consequence, O<sub>2</sub> is fully converted into CO, while CO<sub>2</sub> is not detectable as a product in this case (O<sub>2</sub>\_H).

Figure 9. Densities of free C(s) and occupied C(s)-O active sites as a function of the carbon bed length for the O<sub>2</sub>\_H test.

Therefore, we can divide the carbon bed in two zones: zone 1 where  $O_2$  is depleted and carbon is primarily oxidized to  $CO_2$ , and zone 2 where  $CO_2$  is consumed via the RBR. The length of the two zones depends on the temperature and the oxygen coverage ( $C(s)-O/C(s)$ ) of the carbon surface. Indeed, despite the fact that the oxidation reactions typically occur within a few millimetres in the carbon bed (see Figure S10 and S11 in SI), the deactivation may start earlier than the substantial depletion of the pellets.

In order to get more insights into the deactivation mechanism, we simulated the gasification process after 10 minutes of treatment ( $O_2-H_{600}$ ). The experiments displayed that the carbon bed was no longer able to completely convert the  $CO_2$  produced by the oxidation reactions through the RBR, due to both the reduced length of the bed (0.718 cm) and the saturation in oxygen of the surface. Indeed, in order to predict simultaneously a quantitative conversion of  $O_2$  and the presence of  $CO_2$  in the products, 11 % of oxygen coverage at the surface has been added in the model. Without such addition,  $O_2$  is not fully consumed by the oxidation of the oxygen complexes and only CO is produced. According to Figure 9, we can reasonably assume that oxygen coverage builds up. The reaction analysis for  $O_2-H_{600}$  (see Figure S12 in SI) indicates that  $O_2$  chemisorption rapidly slows down until  $O_2$  is released instead, due to oxygen coverage at the surface. The onset of oxygen coverage with consequent release of  $O_2$  favours the formation of  $CO_2$ . The Boudouard equilibrium is also shifted towards  $CO_2$  production.

Thus, the deactivation of the carbon bed, as observed in our experiments after a few minutes (see Figures 5 and 6 above) can be ascribed to the rapid formation of oxygen complexes at the surface, which undergo both fast oxidation to  $CO_2$  and decomposition to CO. Both reactions efficiently consume solid carbon, reducing the bed size and the zone where  $CO_2$  can react with the active sites. However,  $O_2$  chemisorption is so fast that  $C(s)-O$  oxidation and decomposition are the limiting steps, leaving the surface partially saturated in oxygen. On top of that, the oxygen coverage hinders the sites for  $O_2$  chemisorption, favouring oxidation, which promotes the forward over the reverse Boudouard reaction, producing additional  $CO_2$  at the expense of CO. This explains the drop in  $CO_2$  conversion and in CO concentration after a few minutes in our experiments (see Figures 5 and 6 above).

Figure 8 also shows that when pure  $CO_2$  is introduced as input gas into the reactor tube, the performance of the carbon bed is constant over time. In contrast to  $O_2$ ,  $CO_2$  is unreactive towards solid carbon at temperature lower than about

1000 K [27]. In fact, at 983 K (CO<sub>2</sub>\_C) the production of CO is very small, resulting from the RBR. For similar conditions (O<sub>2</sub>\_E, 1086 K), O<sub>2</sub> is promptly removed from the gas phase.

On the other hand, at 1413 K (CO<sub>2</sub>\_H), the RBR slowly consumes CO<sub>2</sub>, producing CO and oxygen complexes (see Figure S13 in SI). Such complexes release a second CO molecule upon collisions with gas molecules (or O atoms). Since the reaction, CO<sub>2</sub>(g) + C(s) → CO(g) + C(s)-O, proceeds much slower than the O<sub>2</sub> dissociative chemisorption, the RBR is never hindered by oxygen coverage at the surface. Such a slower kinetics is also highlighted by the carbon consumption rates described in Panerai *et al.* [41]. As a result, at this condition more than 80% CO is produced, both in the experiments and predicted by our model (CO<sub>2</sub>\_H).

Finally, CO was tested as feed gas and the experiments confirmed its inertness toward solid carbon, even at high temperature (CO\_C, 1508 K). Indeed, in absence of O/O<sub>2</sub> in the gas phase, oxygen complexes cannot be formed over the surface and CO cannot be oxidized through the forward Boudouard reaction. At the same time, CO does not present any reactivity towards the free active sites.

At this point, we validated our 0D kinetic model for the gasification of carbon under different atmospheres (O<sub>2</sub>, CO<sub>2</sub>, CO, separately) in a wide range of operating conditions. The insights achieved by this set of simulations, performed to reproduce the experimental results from Panerai *et al.* [41], help us to explain the underlying pathways for O/O<sub>2</sub> removal and CO formation, as well as for subsequent carbon bed consumption and deactivation occurring in our experiments. These mechanisms are schematically illustrated in Figure 10, and can be summarized as follows.

When we turn on the plasma, a part of CO<sub>2</sub> undergoes splitting into CO and O. Subsequently, the O atoms will recombine into O<sub>2</sub> and/or react back with CO to form again CO<sub>2</sub>. Therefore, the reactive mixture reaching the carbon pellets will be composed of a combination of CO<sub>2</sub>, CO, O<sub>2</sub> and O. During the first millimetres of the carbon bed, O<sub>2</sub>/O promptly chemisorb at the surface. The reaction is favoured both kinetically and thermodynamically, heating up the first layer of the pellets (see Figure 7). The temperature spikes up to ca. 1700 K and CO desorption can proceed. At such high temperature, CO<sub>2</sub> can also be consumed through the RBR, increasing its conversion and further enhancing the CO production (see Figures 5 and 6).

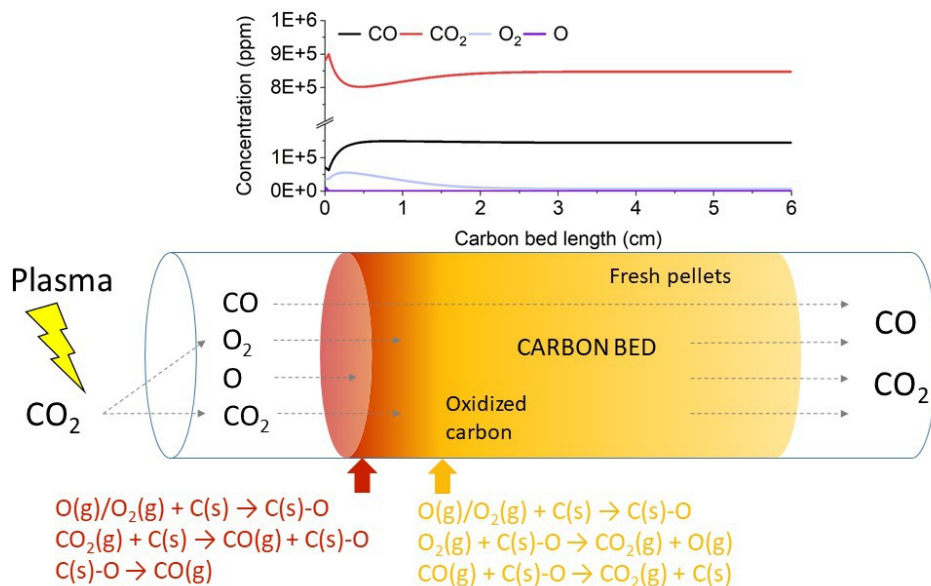
However, O<sub>2</sub>/O chemisorption is faster than C(s)-O oxidation (O<sub>2</sub>(g) + C(s)-O → CO<sub>2</sub>(g) + O(g)) and CO desorption (C(s)-O → CO(g)) and the oxygen coverage at the surface starts to rise. Consequently, oxidation slows down, lowering the temperature, and O<sub>2</sub>/O can reach the bulk of the carbon bed, explaining the increase in temperature further away from the plasma (see Figure 7). The oxygen coverage deactivates the entire bed and CO<sub>2</sub> production is promoted by the full oxidation of the surface (O<sub>2</sub>(g) + C(s)-O → CO<sub>2</sub>(g) + O(g)) and the forward Boudouard reaction (CO(g) + C(s)-O



$\text{CO}_2(\text{g}) + \text{C}(\text{s})$ ). At this point, the  $\text{CO}_2$  concentration is higher than the benchmark, as well as the temperature, due to the exothermic oxidation reactions. Eventually, the oxygen coverage is so important that the carbon bed no longer quenches  $\text{O}_2$ , which can be found in the product composition. As mentioned, the overall mechanism for  $\text{O}/\text{O}_2$  removal and  $\text{CO}$  (as well as  $\text{CO}_2$ ) formation is summarized in Figure 10.

Figure 10. Schematic illustration of the underlying mechanism for  $\text{O}/\text{O}_2$  removal and  $\text{CO}$  (and  $\text{CO}_2$ ) formation in the presence of a carbon bed after a  $\text{CO}_2$  plasma.

Thus, the underlying mechanisms hypothesised based on our experimental observations are in line with the interpretation of our modelling results. In particular, the proposed mechanism demonstrates that the fast drop in



performance of our experimental setup is not caused by a malfunctioning of the silo supplying fresh pellets. Instead, the operating temperature represents a crucial parameter, defining the composition of the gas-phase products and the rate of consumption of the pellets. Following these observations, we believe that providing additional heating to the carbon bed could help reducing the oxygen coverage and promoting the  $\text{CO}$  desorption. In this respect, an additional burner, most likely powered by gas, can purge periodically the amount of spent pellets left in the reactor, favouring the descent of fresh carbon from the silo. Another option can be the use of a thermal plasma, which can provide higher dissociation in the plasma region and, therefore, a more reactive mixture entering the carbon bed, with higher gas temperature, thus increasing conversion and energy efficiency [32,33]. However, as a drawback, argon had to be added to  $\text{CO}_2$  in the feed mixture, in order to maintain the discharge and protect the cathode from carbon contamination [77].

The removal of argon from the product mixture would require additional energy thereby reducing the energy efficiency.

The other studies in literature mentioned earlier on the combination of plasma with carbon bed also reported that  $O/O_2$  is rapidly and easily quenched by the carbon bed, although different carbon materials were used in the various papers, including ours. Note that we have a mesh between our plasma and carbon bed, which was not the case in [32,33]. Hence, the question arises whether this mesh could hinder the plasma coming in contact with the carbon bed. However, this is not the case, because in one plasma run the mesh was actually molten in its center, indicating that the plasma was even attracted towards the center of the mesh, as the latter is conductive. Moreover, if the mesh would cause an obstruction, leading to a lower peak temperature, we would observe that effect from the very beginning of the measurement, while this is not the case (see the experimental temperature profile in Figure 7). Finally, in reference [34], Huang *et al* used an atmospheric non-thermal plasmatron with a stop-mesh on top of the carbon bed, to split the plasma into numerous micro-plasma jets after passing through the mesh. Therefore, adding a mesh at the anode exit is a way to attract the arc toward the outlet, directly towards the carbon bed. Huang *et al.* were able to observe a transient peak in the  $O_2$  online-concentration profile 20 seconds after plasma ignition, that rapidly drops to zero [34], while Li *et al.* didn't detect any oxygen in their experiments [32]. This is indeed very beneficial in terms of separation costs, as mentioned in section 4.1, in addition to the higher CO concentration obtained at these conditions. Hence, the key parameter to reach higher conversion appears to be the temperature, that depends not only on the type of plasma but also on the reactivity of the carbon bed toward  $O/O_2$ , and subsequently the ability of the carbon bed to release heat that can be directly reused to drive the RBR. Thus, future work should focus on searching the "ideal" combination of these parameters (type and size of carbon material, and operating conditions).

## 5. Conclusion

Plasma technology is very promising for  $CO_2$  conversion, and especially warm plasmas, such as gliding arc and microwave plasmas, which exhibit good energy efficiency, but the conversion is subject to further improvement. Moreover,  $CO_2$  is converted into CO and  $O_2$ , which need to be separated in a second stage. In order to enhance the  $CO_2$  conversion after the plasma, as well as the energy efficiency (thus reducing the energy cost), and at the same time promote  $O/O_2$  removal and increase the CO fraction in the exhaust mixture, we placed a carbon bed after a Gliding Arc Plasmatron (GAP) reactor. Carbon pellets were constantly supplied by an innovative (silo) system, to avoid carbon depletion upon reaction with  $O/O_2$ .

This carbon bed allows to significantly enhance the CO<sub>2</sub> conversion, by almost a factor two (from 7.6 % to 12.6 %), while the energy efficiency rises from 27.9 % to 45.4 %, corresponding to a drop in energy cost from 41.9 kJ.L<sup>-1</sup> (without) to 25.4 kJ.L<sup>-1</sup> (with carbon bed). In addition, the CO concentration is about three times higher upon addition of the carbon bed, while the O<sub>2</sub> is nearly completely removed from the exhaust mixture, which is very beneficial, as it simplifies separation costs.

To understand the underlying mechanisms, we measured the temperature as a function of distance from the reactor outlet, and we also monitored the CO<sub>2</sub>, CO and O<sub>2</sub> concentrations, as well as the temperature in the carbon bed, as a function of time. The time-resolved measurements reveal that the CO<sub>2</sub> conversion and CO concentration are only enhanced in the first minutes, followed by a drop to values below the benchmark (i.e., without carbon bed). To better understand this behaviour, we developed a model for the gasification of carbon under the effect of different gases (O<sub>2</sub>, CO and CO<sub>2</sub> separately), which has been successfully validated with published experimental results.

Both our measurements and modelling results reveal that the onset of oxygen coverage at the carbon surface is of crucial importance to define the performance of the conversion process. In particular, the presence of oxygen complexes increases the selectivity towards CO<sub>2</sub> through the C(s)-O oxidation and the forward Boudouard reactions. In other words, the drop in CO<sub>2</sub> conversion and in CO concentration after a few minutes is attributed to the deactivation of the carbon bed, due to rapid formation of oxygen complexes at the surface.

This oxygen coverage can be limited by increasing the temperature in the carbon bed, i.e., by providing additional heating, leading to a complete consumption of the bed, followed by supplying fresh pellets from the silo. Hence, in our future work, we plan to apply additional heating, to further improve the performance. This additional heating will increase the energy cost of the process, linearly with the additional power supplied for the heating. This may lower the overall energy efficiency. However, the latter is not necessarily the case, if the rise in conversion due to the additional heating (promoting the specific chemical reactions) is higher than the increase in energy consumption. We aim to find conditions under which the beneficial effect of additional heating is larger than the additional energy cost. Nevertheless, our present results are already very promising, and clearly demonstrate the large potential of adding a carbon bed after a plasma reactor. In addition, our model provides very useful insights that explain our experimental observations and that are also useful for other experimental groups.

## **Acknowledgments**

This research was supported by the European Research Council (ERC) under the European Union's Horizon 2020 Research and Innovation programme (grant agreement No 810182 – SCOPE ERC Synergy project) and the European Union's Horizon 2020 Research and Innovation programme under the Marie Skłodowska-Curie grant agreement No 813393 (PIONEER). The calculations were performed using the Turing HPC infrastructure at the CalcUA core facility of the Universiteit Antwerpen (UAntwerpen), a division of the Flemish Supercomputer Center VSC, funded by the Hercules Foundation, the Flemish Government (department EWI) and the UAntwerpen. We also thank R. De Meyer, K. Leyssens and S. Defossé for performing the charcoal characterizations.

### **Conflict of interest**

The authors have no conflicts of interest to declare.

### **Author information**

F.G-S and A.B. developed the concept of this study, F.G-S designed the setup and performed the experiments. O. B. developed the model. F.G-S., O.B. and A.B. co-wrote the manuscript. All authors discussed the results and approved the manuscript.

### **References**

- [1] J. Godin, W. Liu, S. Ren, C.C. Xu, Advances in recovery and utilization of carbon dioxide: A brief review, *Journal of Environmental Chemical Engineering*. 9 (2021) 105644. <https://doi.org/10.1016/j.jece.2021.105644>.
- [2] S.J. Davis, N.S. Lewis, M. Shaner, S. Aggarwal, D. Arent, I.L. Azevedo, S.M. Benson, T. Bradley, J. Brouwer, Y.-M. Chiang, C.T.M. Clack, A. Cohen, S. Doig, J. Edmonds, P. Fennell, C.B. Field, B. Hannegan, B.-M. Hodge, M.I. Hoffert, E. Ingersoll, P. Jaramillo, K.S. Lackner, K.J. Mach, M. Mastrandrea, J. Ogden, P.F. Peterson, D.L. Sanchez, D. Sperling, J. Stagner, J.E. Trancik, C.-J. Yang, K. Caldeira, Net-zero emissions energy systems, *Science*. 360 (2018) eaas9793. <https://doi.org/10.1126/science.aas9793>.
- [3] A. Hassanpouryouzband, E. Joonaki, K. Edlmann, R.S. Haszeldine, Offshore Geological Storage of Hydrogen: Is This Our Best Option to Achieve Net-Zero?, *ACS Energy Lett*. 6 (2021) 2181–2186. <https://doi.org/10.1021/acsenergylett.1c00845>.
- [4] R. Snoeckx, A. Bogaerts, Plasma technology – a novel solution for CO<sub>2</sub> conversion?, *Chem. Soc. Rev*. 46 (2017) 5805–5863. <https://doi.org/10.1039/C6CS00066E>.
- [5] A. Bogaerts, X. Tu, G. van Rooij, R. van de Sanden, 28. Plasma-based CO<sub>2</sub> conversion, in: M. North, P. Styring (Eds.), *Transformations*, De Gruyter, Berlin, Boston, 2019: pp. 585–634. <https://doi.org/10.1515/9783110665147-028>.
- [6] R. Aerts, R. Snoeckx, A. Bogaerts, In-Situ Chemical Trapping of Oxygen in the Splitting of Carbon Dioxide by Plasma: In-Situ Chemical Trapping of O<sub>2</sub> in CO<sub>2</sub>

- Splitting by DBD, *Plasma Process. Polym.* 11 (2014) 985–992. <https://doi.org/10.1002/ppap.201400091>.
- [7] R. Aerts, W. Somers, A. Bogaerts, Carbon Dioxide Splitting in a Dielectric Barrier Discharge Plasma: A Combined Experimental and Computational Study, *ChemSusChem*. 8 (2015) 702–716. <https://doi.org/10.1002/cssc.201402818>.
- [8] M. Ramakers, I. Michielsens, R. Aerts, V. Meynen, A. Bogaerts, Effect of Argon or Helium on the CO<sub>2</sub> Conversion in a Dielectric Barrier Discharge: Effect of argon or helium on the CO<sub>2</sub> conversion in a dielectric barrier discharge, *Plasma Process. Polym.* 12 (2015) 755–763. <https://doi.org/10.1002/ppap.201400213>.
- [9] A. Fridman, A. Chirokov, A. Gutsol, Non-thermal atmospheric pressure discharges, *J. Phys. D: Appl. Phys.* 38 (2005) R1–R24. <https://doi.org/10.1088/0022-3727/38/2/R01>.
- [10] L.D. Pietanza, G. Colonna, M. Capitelli, Kinetics versus thermodynamics on CO<sub>2</sub> dissociation in high temperature microwave discharges, *Plasma Sources Sci. Technol.* 29 (2020) 035022. <https://doi.org/10.1088/1361-6595/ab6e5a>.
- [11] T. Silva, N. Britun, T. Godfroid, R. Snyders, Understanding CO<sub>2</sub> decomposition in microwave plasma by means of optical diagnostics, *Plasma Process Polym.* 14 (2017) 1600103. <https://doi.org/10.1002/ppap.201600103>.
- [12] N. den Harder, D.C.M. van den Bekerom, R.S. Al, M.F. Graswinckel, J.M. Palomares, F.J.J. Peeters, S. Ponduri, T. Minea, W.A. Bongers, M.C.M. van de Sanden, G.J. van Rooij, Homogeneous CO<sub>2</sub> conversion by microwave plasma: Wave propagation and diagnostics, *Plasma Process Polym.* 14 (2017) 1600120. <https://doi.org/10.1002/ppap.201600120>.
- [13] W. Wang, D. Mei, X. Tu, A. Bogaerts, Gliding arc plasma for CO<sub>2</sub> conversion: Better insights by a combined experimental and modelling approach, *Chemical Engineering Journal*. 330 (2017) 11–25. <https://doi.org/10.1016/j.cej.2017.07.133>.
- [14] Ts. Paunskas, G. Trenchev, A. Bogaerts, St. Kolev, A 2D model of a gliding arc discharge for CO<sub>2</sub> conversion, in: Sofia, Bulgaria, 2019: p. 060008. <https://doi.org/10.1063/1.5091186>.
- [15] G. Trenchev, A. Nikiforov, W. Wang, St. Kolev, A. Bogaerts, Atmospheric pressure glow discharge for CO<sub>2</sub> conversion: Model-based exploration of the optimum reactor configuration, *Chemical Engineering Journal*. 362 (2019) 830–841. <https://doi.org/10.1016/j.cej.2019.01.091>.
- [16] M. Grofulović, B.L.M. Klarenaar, O. Guaitella, V. Guerra, R. Engeln, A rotational Raman study under non-thermal conditions in pulsed CO<sub>2</sub>-N<sub>2</sub> and CO<sub>2</sub>-O<sub>2</sub> glow discharges, *Plasma Sources Science and Technology*. 28 (2019) 045014. <https://doi.org/10.1088/1361-6595/ab1240>.
- [17] L. Terraz, T. Silva, A. Morillo-Candas, O. Guaitella, A. Tejero-del-Caz, L.L. Alves, V. Guerra, Influence of N<sub>2</sub> on the CO<sub>2</sub> vibrational distribution function and dissociation yield in non-equilibrium plasmas, *Journal of Physics D: Applied Physics*. 53 (2019) 094002. <https://doi.org/10.1088/1361-6463/ab55fb>.
- [18] M. Ramakers, S. Heijkers, T. Tytgat, S. Lenaerts, A. Bogaerts, Combining CO<sub>2</sub> conversion and N<sub>2</sub> fixation in a gliding arc plasmatron, *Journal of CO<sub>2</sub> Utilization*. 33 (2019) 121–130. <https://doi.org/10.1016/j.jcou.2019.05.015>.
- [19] H. Zhang, L. Li, X. Li, W. Wang, J. Yan, X. Tu, Warm plasma activation of CO<sub>2</sub> in a rotating gliding arc discharge reactor, *Journal of CO<sub>2</sub> Utilization*. 27 (2018) 472–479. <https://doi.org/10.1016/j.jcou.2018.08.020>.
- [20] R. Snoeckx, S. Heijkers, K. Van Wesenbeeck, S. Lenaerts, A. Bogaerts, CO<sub>2</sub> conversion in a dielectric barrier discharge plasma: N<sub>2</sub> in the mix as a helping

- hand or problematic impurity?, *Energy & Environmental Science*. 9 (2016) 999–1011. <https://doi.org/10.1039/C5EE03304G>.
- [21] P.V. Ananthapadmanabhan, N. Venkatramani, Chapter 6 Thermal plasma processing, in: C. Suryanarayana (Ed.), *Non-Equilibrium Processing of Materials*, Pergamon, 1999: pp. 121–150. [https://doi.org/10.1016/S1470-1804\(99\)80052-2](https://doi.org/10.1016/S1470-1804(99)80052-2).
- [22] A. Bogaerts, E. Neyts, R. Gijbels, J. van der Mullen, Gas discharge plasmas and their applications, *Spectrochimica Acta Part B: Atomic Spectroscopy*. 57 (2002) 609–658. [https://doi.org/10.1016/S0584-8547\(01\)00406-2](https://doi.org/10.1016/S0584-8547(01)00406-2).
- [23] B. Wang, Z. Song, L. Sun, A review: Comparison of multi-air-pollutant removal by advanced oxidation processes – Industrial implementation for catalytic oxidation processes, *Chemical Engineering Journal*. 409 (2021) 128136. <https://doi.org/10.1016/j.cej.2020.128136>.
- [24] F. Rezaei, P. Vanraes, A. Nikiforov, R. Morent, N. De Geyter, Applications of Plasma-Liquid Systems: A Review, *Materials*. 12 (2019). <https://doi.org/10.3390/ma12172751>.
- [25] H. Tian, Q. Hu, J. Wang, D. Chen, Y. Yang, A.V. Bridgwater, Kinetic study on the CO<sub>2</sub> gasification of biochar derived from *Miscanthus* at different processing conditions, *Energy*. 217 (2021) 119341. <https://doi.org/10.1016/j.energy.2020.119341>.
- [26] W. Kwapinski, C.M.P. Byrne, E. Kryachko, P. Wolfram, C. Adley, J.J. Leahy, E.H. Novotny, M.H.B. Hayes, Biochar from Biomass and Waste, *Waste Biomass Valor*. 1 (2010) 177–189. <https://doi.org/10.1007/s12649-010-9024-8>.
- [27] P. Lahijani, Z.A. Zainal, M. Mohammadi, A.R. Mohamed, Conversion of the greenhouse gas CO<sub>2</sub> to the fuel gas CO via the Boudouard reaction: A review, *Renewable and Sustainable Energy Reviews*. 41 (2015) 615–632. <https://doi.org/10.1016/j.rser.2014.08.034>.
- [28] H. Dai, H. Zhao, S. Chen, B. Jiang, A Microwave-Assisted Boudouard Reaction: A Highly Effective Reduction of the Greenhouse Gas CO<sub>2</sub> to Useful CO Feedstock with Semi-Coke, *Molecules*. 26 (2021) 1507. <https://doi.org/10.3390/molecules26061507>.
- [29] J. Hunt, A. Ferrari, A. Lita, M. Crosswhite, B. Ashley, A.E. Stiegman, Microwave-Specific Enhancement of the Carbon–Carbon Dioxide (Boudouard) Reaction, *J. Phys. Chem. C*. 117 (2013) 26871–26880. <https://doi.org/10.1021/jp4076965>.
- [30] J.A. Menéndez, A. Domínguez, Y. Fernández, J.J. Pis, Evidence of Self-Gasification during the Microwave-Induced Pyrolysis of Coffee Hulls, *Energy Fuels*. 21 (2007) 373–378. <https://doi.org/10.1021/ef060331i>.
- [31] R. Roncancio, J.P. Gore, CO<sub>2</sub> char gasification: A systematic review from 2014 to 2020, *Energy Conversion and Management*: X. 10 (2021) 100060. <https://doi.org/10.1016/j.ecmx.2020.100060>.
- [32] Z. Li, T. Yang, S. Yuan, Y. Yin, E.J. Devid, Q. Huang, D. Auerbach, A.W. Kleyn, Boudouard reaction driven by thermal plasma for efficient CO<sub>2</sub> conversion and energy storage, *Journal of Energy Chemistry*. 45 (2020) 128–134. <https://doi.org/10.1016/j.jechem.2019.10.007>.
- [33] P. Liu, X. Liu, J. Shen, Y. Yin, T. Yang, Q. Huang, D. Auerbach, A.W. Kleyn, CO<sub>2</sub> conversion by thermal plasma with carbon as reducing agent: high CO yield and energy efficiency, *Plasma Sci. Technol.* 21 (2019) 012001. <https://doi.org/10.1088/2058-6272/aadf30>.
- [34] J. Huang, H. Zhang, Q. Tan, L. Li, R. Xu, Z. Xu, X. Li, Enhanced conversion of CO<sub>2</sub> into O<sub>2</sub>-free fuel gas via the Boudouard reaction with biochar in an atmospheric plasmatron, *Journal of CO<sub>2</sub> Utilization*. 45 (2021) 101429. <https://doi.org/10.1016/j.jcou.2020.101429>.

- [35] V. Vermeiren, A. Bogaerts, Plasma-Based CO<sub>2</sub> Conversion: To Quench or Not to Quench?, *J. Phys. Chem. C*. 124 (2020) 18401–18415. <https://doi.org/10.1021/acs.jpcc.0c04257>.
- [36] V. Givotov, A. Fridman, M. Krotov, E. Krasheninnikov, B. Patrushev, V. Rusanov, G. Sholin, Plasmochemical methods of hydrogen production, *International Journal of Hydrogen Energy*. 6 (1981) 441–449. [https://doi.org/10.1016/0360-3199\(81\)90076-8](https://doi.org/10.1016/0360-3199(81)90076-8).
- [37] G.J. van Rooij, H.N. Akse, W.A. Bongers, M.C.M. van de Sanden, Plasma for electrification of chemical industry: a case study on CO<sub>2</sub> reduction, *Plasma Phys. Control. Fusion*. 60 (2018) 014019. <https://doi.org/10.1088/1361-6587/aa8f7d>.
- [38] G. Chen, F. Buck, I. Kistner, M. Widenmeyer, T. Schiestel, A. Schulz, M. Walker, A. Weidenkaff, A novel plasma-assisted hollow fiber membrane concept for efficiently separating oxygen from CO in a CO<sub>2</sub> plasma, *Chemical Engineering Journal*. 392 (2020) 123699. <https://doi.org/10.1016/j.cej.2019.123699>.
- [39] M. Ramakers, G. Trenchev, S. Heijkers, W. Wang, A. Bogaerts, Gliding Arc Plasmatron: Providing an Alternative Method for Carbon Dioxide Conversion, *ChemSusChem*. 10 (2017) 2642–2652. <https://doi.org/10.1002/cssc.201700589>.
- [40] L.L. Alves, A. Bogaerts, V. Guerra, M.M. Turner, Foundations of modelling of nonequilibrium low-temperature plasmas, *Plasma Sources Sci. Technol.* 27 (2018) 023002. <https://doi.org/10.1088/1361-6595/aaa86d>.
- [41] F. Panerai, T. Cochell, A. Martin, J.D. White, Experimental measurements of the high-temperature oxidation of carbon fibers, *International Journal of Heat and Mass Transfer*. 136 (2019) 972–986. <https://doi.org/10.1016/j.ijheatmasstransfer.2019.03.018>.
- [42] T. Nunnally, K. Gutsol, A. Rabinovich, A. Fridman, A. Gutsol, A. Kemoun, Dissociation of CO<sub>2</sub> in a low current gliding arc plasmatron, *J. Phys. D: Appl. Phys.* 44 (2011) 274009. <https://doi.org/10.1088/0022-3727/44/27/274009>.
- [43] M. Ramakers, J.A. Medrano, G. Trenchev, F. Gallucci, A. Bogaerts, Revealing the arc dynamics in a gliding arc plasmatron: a better insight to improve CO<sub>2</sub> conversion, *Plasma Sources Sci. Technol.* 26 (2017) 125002. <https://doi.org/10.1088/1361-6595/aa9531>.
- [44] G. Trenchev, St. Kolev, W. Wang, M. Ramakers, A. Bogaerts, CO<sub>2</sub> Conversion in a Gliding Arc Plasmatron: Multidimensional Modeling for Improved Efficiency, *J. Phys. Chem. C*. 121 (2017) 24470–24479. <https://doi.org/10.1021/acs.jpcc.7b08511>.
- [45] S. Pancheshnyi, B. Eismann, G. Hagelaar, L. Pitchford, Computer Code ZDPlasKin, 2008. <http://www.zdplaskin.laplace.univ-tlse.fr>.
- [46] B. McEnaney, Active Sites in Relation to Gasification of Coal Chars, in: J. Lahaye, P. Ehrburger (Eds.), *Fundamental Issues in Control of Carbon Gasification Reactivity*, Springer Netherlands, Dordrecht, 1991: pp. 175–203. [https://doi.org/10.1007/978-94-011-3310-4\\_10](https://doi.org/10.1007/978-94-011-3310-4_10).
- [47] K.S. Prata, T.E. Schwartzentruber, T.K. Minton, Air–Carbon Ablation Model for Hypersonic Flight from Molecular-Beam Data, *AIAA Journal*. (2021) 1–14. <https://doi.org/10.2514/1.J060516>.
- [48] C. Park, Effects of atomic oxygen on graphite ablation, *AIAA Journal*. 14 (1976) 1640–1642. <https://doi.org/10.2514/3.7267>.
- [49] S.V. Zhluktov, T. Abe, Viscous Shock-Layer Simulation of Airflow past Ablating Blunt Body with Carbon Surface, *Journal of Thermophysics and Heat Transfer*. 13 (1999) 50–59. <https://doi.org/10.2514/2.6400>.
- [50] S. Poovathingal, T.E. Schwartzentruber, V.J. Murray, T.K. Minton, G.V. Candler, Finite-Rate Oxidation Model for Carbon Surfaces from Molecular

- Beam Experiments, *AIAA Journal*. 55 (2017) 1644–1658.  
<https://doi.org/10.2514/1.J055371>.
- [51] F.J. Vastola, P.L. Walker, R.O. Lussow, KINETICS OF OXYGEN INTERACTION WITH GRAPHON BETWEEN 450 AND 675°C”, *Carbon*. 5 (1967) 12.
- [52] S. Ahmed, M.H. Back, J.M. Roscoe, A kinetic model for the low temperature oxidation of carbon: I, *Combustion and Flame*. 70 (1987) 1–16.  
[https://doi.org/10.1016/0010-2180\(87\)90155-6](https://doi.org/10.1016/0010-2180(87)90155-6).
- [53] L.R. Radovic, Active Sites in Graphene and the Mechanism of CO<sub>2</sub> Formation in Carbon Oxidation, *J. Am. Chem. Soc.* 131 (2009) 17166–17175.  
<https://doi.org/10.1021/ja904731q>.
- [54] L.R. Radovic, A. Suarez, F. Vallejos-Burgos, J.O. Sofo, Oxygen migration on the graphene surface. 2. Thermochemistry of basal-plane diffusion (hopping), *Carbon*. 49 (2011) 4226–4238.  
<https://doi.org/10.1016/j.carbon.2011.05.037>.
- [55] K.S. Prata, T.E. Schwartzentruber, T.K. Minton, Air–Carbon Ablation Model for Hypersonic Flight from Molecular-Beam Data, *AIAA Journal*. 60 (2022) 627–640. <https://doi.org/10.2514/1.J060516>.
- [56] K.L. Yang, R.T. Yang, Absolute rates of the carbon-carbon dioxide reaction, *AIChE J.* 31 (1985) 1313–1321. <https://doi.org/10.1002/aic.690310810>.
- [57] G. Tremblay, F.J. Vastola, P.L. Walker, Thermal desorption analysis of oxygen surface complexes on carbon, *Carbon*. 16 (1978) 35–39.  
[https://doi.org/10.1016/0008-6223\(78\)90113-6](https://doi.org/10.1016/0008-6223(78)90113-6).
- [58] A. Montoya, T.-T.T. Truong, F. Mondragón, T.N. Truong, CO Desorption from Oxygen Species on Carbonaceous Surface: 1. Effects of the Local Structure of the Active Site and the Surface Coverage, *J. Phys. Chem. A*. 105 (2001) 6757–6764. <https://doi.org/10.1021/jp010572l>.
- [59] F. Panerai, J.C. Ferguson, J. Lachaud, A. Martin, M.J. Gasch, N.N. Mansour, Micro-tomography based analysis of thermal conductivity, diffusivity and oxidation behavior of rigid and flexible fibrous insulators, *International Journal of Heat and Mass Transfer*. 108 (2017) 801–811.  
<https://doi.org/10.1016/j.ijheatmasstransfer.2016.12.048>.
- [60] R. Jambunathan, D.A. Levin, A. Borner, J.C. Ferguson, F. Panerai, Prediction of gas transport properties through fibrous carbon preform microstructures using Direct Simulation Monte Carlo, *International Journal of Heat and Mass Transfer*. 130 (2019) 923–937.  
<https://doi.org/10.1016/j.ijheatmasstransfer.2018.11.006>.
- [61] N. Nouri, F. Panerai, K.A. Tagavi, N.N. Mansour, A. Martin, Evaluation of the anisotropic radiative conductivity of a low-density carbon fiber material from realistic microscale imaging, *International Journal of Heat and Mass Transfer*. 95 (2016) 535–539.  
<https://doi.org/10.1016/j.ijheatmasstransfer.2015.12.004>.
- [62] A.V. Gusarov, E. Poloni, V. Shklover, A. Sologubenko, J. Leuthold, S. White, J. Lawson, Radiative transfer in porous carbon-fiber materials for thermal protection systems, *International Journal of Heat and Mass Transfer*. 144 (2019) 118582. <https://doi.org/10.1016/j.ijheatmasstransfer.2019.118582>.
- [63] I.M.K. Ismail, Structure and active surface area of carbon fibers, *Carbon*. 25 (1987) 653–662. [https://doi.org/10.1016/0008-6223\(87\)90219-3](https://doi.org/10.1016/0008-6223(87)90219-3).
- [64] A. Fukunaga, T. Komami, S. Ueda, M. Nagumo, Plasma treatment of pitch-based ultra high modulus carbon fibers, *Carbon*. 37 (1999) 1087–1091.  
[https://doi.org/10.1016/S0008-6223\(98\)00308-X](https://doi.org/10.1016/S0008-6223(98)00308-X).
- [65] P. Lahijani, Z.A. Zainal, M. Mohammadi, A.R. Mohamed, Conversion of the greenhouse gas CO<sub>2</sub> to the fuel gas CO via the Boudouard reaction: A review,



- Renewable and Sustainable Energy Reviews. 41 (2015) 615–632.  
<https://doi.org/10.1016/j.rser.2014.08.034>.
- [66] J.M. Bermúdez, E. Ruisánchez, A. Arenillas, A.H. Moreno, J.A. Menéndez, New concept for energy storage: Microwave-induced carbon gasification with CO<sub>2</sub>, *Energy Conversion and Management*, 78 (2014) 559–564.  
<https://doi.org/10.1016/j.enconman.2013.11.021>.
- [67] P. Geng, Y. Zhang, Z. Liu, L. Liao, R. Liu, J. Zheng, Further insights into the effect of the mass transfer limitations on the reaction order of the char-CO<sub>2</sub> reaction, *Thermochimica Acta*, 680 (2019) 178349.  
<https://doi.org/10.1016/j.tca.2019.178349>.
- [68] F. Mermoud, F. Golfier, S. Salvador, L.V. de Steene, J.L. Dirion, Experimental and numerical study of steam gasification of a single charcoal particle, *Combustion and Flame*, 145 (2006) 59–79.  
<https://doi.org/10.1016/j.combustflame.2005.12.004>.
- [69] A. Ferrari, J. Hunt, A. Lita, B. Ashley, A.E. Stiegman, Microwave-Specific Effects on the Equilibrium Constants and Thermodynamics of the Steam-Carbon and Related Reactions, *J. Phys. Chem. C*, 118 (2014) 9346–9356.  
<https://doi.org/10.1021/jp501206n>.
- [70] H.P. Boehm, Surface oxides on carbon and their analysis: a critical assessment, *Carbon*, 40 (2002) 145–149. [https://doi.org/10.1016/S0008-6223\(01\)00165-8](https://doi.org/10.1016/S0008-6223(01)00165-8).
- [71] A.F. Dias Junior, R.P. Esteves, Á.M. da Silva, A.D. Sousa Júnior, M.P. Oliveira, J.O. Brito, A. Napoli, B.M. Braga, Investigating the pyrolysis temperature to define the use of charcoal, *European Journal of Wood and Wood Products*, 78 (2020) 193–204. <https://doi.org/10.1007/s00107-019-01489-6>.
- [72] E.S. Hecht, C.R. Shaddix, A. Molina, B.S. Haynes, Effect of CO<sub>2</sub> gasification reaction on oxy-combustion of pulverized coal char, *Proceedings of the Combustion Institute*, 33 (2011) 1699–1706.  
<https://doi.org/10.1016/j.proci.2010.07.087>.
- [73] A. Sánchez, F. Mondragón, Role of the Epoxy Group in the Heterogeneous CO<sub>2</sub> Evolution in Carbon Oxidation Reactions, *J. Phys. Chem. C*, 111 (2007) 612–617. <https://doi.org/10.1021/jp065701i>.
- [74] E.S. Hecht, C.R. Shaddix, J.S. Lighty, Analysis of the errors associated with typical pulverized coal char combustion modeling assumptions for oxy-fuel combustion, *Combustion and Flame*, 160 (2013) 1499–1509.  
<https://doi.org/10.1016/j.combustflame.2013.02.015>.
- [75] K. Palacio, A. Sanchez, J.F. Espinal, Thermodynamic evaluation of carbon dioxide gasification reactions at oxy-combustion conditions, *Combustion Science and Technology*, 190 (2018) 1515–1527.  
<https://doi.org/10.1080/00102202.2018.1454916>.
- [76] W.-H. Chen, C.-L. Hsu, S.-W. Du, Thermodynamic analysis of the partial oxidation of coke oven gas for indirect reduction of iron oxides in a blast furnace, *Energy*, 86 (2015) 758–771.  
<https://doi.org/10.1016/j.energy.2015.04.087>.
- [77] Y. Yin, T. Yang, Z. Li, E. Devid, D. Auerbach, A.W. Kleyn, CO<sub>2</sub> conversion by plasma: how to get efficient CO<sub>2</sub> conversion and high energy efficiency, *Phys. Chem. Chem. Phys.* 23 (2021) 7974–7987.  
<https://doi.org/10.1039/D0CP05275B>.

